Ammonia synthesis over cesium-promoted mesoporous-carbon-supported ruthenium catalysts: Impact of graphitization degree of the carbon support

Shih-Yuan Chen [a,*], Li-Yu Wang [b,1], Kai-Chun Chen [b,1], Cheng-Hsi Yeh [c,1], Wei-Chih Hsiao [b,1], Hsin-Yu Chen [d], Masayasu Nishi [a], Martin Keller [e], Chih-Li Chang [f], Chien-Neng Liao [d], Takehisa Mochizuki [a], Hsin-Yi Tiffany Chen [c,d,g,**], Ho-Hsiu Chou [f,*], Chia-Min Yang [b,g,**]

[a] Energy Catalyst Technology Group, Energy Process Research Institute (EPRI), National Institute of Advanced Industrial Science and Technology (AIST), Tsukuba, Ibaraki 305-8559, Japan
[b] Department of Chemistry, National Tsing Hua University, Hsinchu 300044, Taiwan
[c] Department of Engineering and System Science, National Tsing Hua University, Hsinchu 300044, Taiwan
[d] Department of Materials Science and Engineering, National Tsing Hua University, Hsinchu 300044, Taiwan
[e] Smart CO2 Utilization Research Team, Global Zero Emission Research Center (GZR), AIST, 16-1 Onogawa, Tsukuba, Ibaraki 305-8559, Japan
[f] Department of Chemical Engineering, National Tsing Hua University, Hsinchu 300044, Taiwan
[g] College of Semiconductor Research, National Tsing Hua University, Hsinchu 300044, Taiwan

ARTICLE INFO

ABSTRACT

Carbon-supported ruthenium catalysts facilitate electrically-assisted Haber–Bosch ammonia synthesis. However, the relationship between carbon supports and catalytic performance remains ambiguous. We developed ordered mesoporous carbon plates (MCPs) with varying graphitization degrees as Cs-promoted Ru catalyst supports, examining correlations between ammonia synthesis rate and key structural parameters, included graphitization degree, Ru nanoparticle size, and Cs/Ru ratio. High-graphitization-degree carbon supports resisted methanation and facilitated formation of reductive activation enabled dynamic Cs^0 species as electronic promotor, induced by spillover hydrogen from the Ru surface to CsOH. Density functional theory calculations further revealed that CsOH alleviated hydrogen poisoning. Notably, the catalyst supported on MCP-1100—which exhibited the highest graphitization degree among the supports and superior stability—with 10 wt% 2.3-nm-sized Ru nanoparticles and Cs/Ru = 2.5 achieved high ambient-pressure ammonia synthesis rates (7.9–43 $mmol_{NH3} \cdot g^{-1} \cdot h^{-1}$) below 410 °C. Furthermore, it functioned under intermittent operating conditions, potentially integrating renewable-electricity-based electrolytic hydrogen production.

1. Introduction

Ammonia is an essential chemical for the agricultural and chemical industries [1]. Recently, it has been recognized as a promising energy carrier and fuel for realizing an advanced low-carbon society [2]. Large-scale NH_3 synthesis is currently achieved using the Haber–Bosch (HB) process, which involves reacting H_2 and N_2 over promoted Fe catalysts under extreme conditions (~500 °C and ~10–30 MPa) [3]. The

required H_2 is mostly obtained via steam reforming of methane, followed by the water-gas shift reaction and subsequent processes [4]. However, this "gray" H_2 production scheme accounts for ~2% of the global energy consumption and 420 Mt of annual CO_2 emissions [5]. In contrast, "green" H_2 can be produced via water electrolysis using renewable sources (such as wind and solar energy) and then employed in the electrically enhanced HB (eHB) process, enabling "green" NH_3 production with negligible CO_2 emissions [6]. The cost of green NH_3

production through the eHB process is expected to reach that of gray NH$_3$ production achieved using the conventional HB scheme in 2030–2040; importantly, the former generates considerably lower CO$_2$ emissions than those of the latter [7]. However, the production capacity and operating conditions of the eHB process can vary owing to the use of intermittent renewable energy [8]. Specifically, the development of highly active catalysts that can quickly respond to the startup and shutdown stages of the eHB process is a major challenge.

Around the end of the last century, Ru-based catalysts promoted by alkaline and alkaline earth metals were discovered to outperform Fe-based catalysts; these systems have been considered second-generation catalysts in the Kellogg Advanced Ammonia Process (KAAP) for mild ammonia synthesis [9]. Commercial KAAP catalysts contain Ru nanoparticles (NPs) with Cs or Ba promoters on high-surface-area graphite [10]. According to Brown *et al.*, KAAP catalysts are ~10–20 times more active than Fe-based catalysts under similar operating conditions [11]. However, this comparison is inadequate because the two types of catalysts exhibit different kinetic properties and behave differently during ammonia synthesis. Recently, carbon-supported Ru catalysts have been highlighted as being viable for the eHB process because they can catalyze the reaction under relatively mild conditions (<400 °C) and respond rapidly to changes in the operation conditions during intermittent ammonia synthesis [12,13]. Previously reported carbon-supported Ru catalysts exhibiting optimal performance and the corresponding reaction conditions are listed in Table 1 [14–23]. Comparison with additional selected reports is shown in Table S1. These catalysts typically comprise 2–3-nm-sized Ru NPs with multiple electronic or structural promoters as the active components [24,25]. Their ammonia synthesis activity varies considerably from 0.8 to 68 mmol g^{-1} h^{-1} (turnover frequency (TOF) < 0.3 s^{-1}; NH$_3$ yield = 0.75–15.6%) for temperatures, pressures, and gas hourly space velocities (GHSVs) of 275–400 °C, 0.1–10 MPa, and 637–50,000 h^{-1}, respectively. The ammonia synthesis rate is significantly influenced by factors such as the Ru particle size, type of promoter, reaction conditions, and type of carbon support. Distinct from nanoparticle-type Ru catalysts, highly active cluster-type Ru catalysts with or without specific promoter (e.g. Ba) and/or dopant (e.g. Co) were reported by the groups of Wang and Jiang [26,27]. Kowalczyk *et al.* demonstrated that Cs, as a promotor, is more effective in boosting ammonia synthesis than K under the studied conditions [15]. Raróg *et al.* [28] and Siporin *et al.* [29] independently

reported that the Ru catalysts promoted by alkali elements (e.g. Cs) may be less sensitive to the concentration of yielded NH$_3$ and reaction pressure compared with the analogs promoted by alkaline earth metals (e.g. Ba) or rare-earth elements (e.g. La). Comparing catalysts with different carbon supports is a particularly difficult endeavor, because the supports exhibit various degrees of graphitization and different structural/textural properties. Furthermore, these characteristics can be further altered by doping (for example, with nitrogen [18]) or by applying post-treatment strategies (for instance, with nitric acid to generate oxygen-containing functional groups [20]), making it even more challenging to correlate the properties of carbon supports with the activity of supported Ru catalysts. Thermal treatments of carbon materials may positively impact the ammonia synthesis activity of resulting promoted Ru catalysts [17,30]. Additionally, these properties may be directly or indirectly associated with the stability of the catalysts during ammonia synthesis, because carbon-supported Ru catalysts are typically deactivated by sintering of Ru NPs and methanation of carbon supports, likely catalyzed by Ru with spillover hydrogen atoms [30,31].

Our recent studies on Cs-promoted carbon-supported Ru catalysts have indicated that catalysts supported on commercial carbon supports of disordered mesoporous carbon, produced using the hard-template method, and single-wall carbon nanotubes, produced using the super growth method, exhibit higher activities for ammonia synthesis than those of their activated-carbon-supported counterparts [21,23] and drive the reaction at temperatures below 400 °C, thereby inhibiting the metal sintering and carbon support methanation. However, the utilization of carbon supports with distinct degrees of graphitization and structural/textural properties has hindered researchers from establishing correlations between these characteristics and the catalytic performance. Therefore, systematic control and investigation of each structural factor of the carbon support are crucial for acquiring greater insight into the mechanism underlying the reaction and deactivation of ammonia synthesis over carbon-supported Ru catalysts and for enabling rational design of advanced commercial catalysts. To that end, a series of ordered mesoporous carbon plates (MCPs) with similar textural properties but different degrees of graphitization was synthesized in this study and then used as the support to prepare Cs-promoted Ru catalysts. First, the catalysts were optimized for ammonia synthesis under ambient pressure by thoroughly investigating the degree of graphitization of the MCPs and the Ru and Cs loadings to establish correlations with the

Table 1
Comparison of ammonia synthesis activity of 2.5Cs-10Ru/MCP with previously reported carbon-supported Ru catalysts.

Entry	Support[a]	S$_{BET}$ (m$^2 \cdot$g^{-1})	Ru (wt %)	Cs/Ru (molar ratio)	K/Ru (molar ratio)	Ba/Ru (molar ratio)	Reaction condition			NH$_3$ (vol%)	Rate (mmol g^{-1} h^{-1})	TOF (s^{-1})	Ref.
							P (MPa)	Temp. (°C)	GHSV[b] (h^{-1})				
1	MCP	333	10	2.5	-	-	0.1	370	6000	0.90	14.6	0.015	this study
2	MCP	333	10	2.5	-	-	0.9	410	6000	2.72	42.8	0.046	this study
3	CCA	-	4.8	5.0	-	0.5	0.1	275	-	0.75	-	0.001	14
4	AC	-	9.1	-	3.7	-	10	400	55000	1.90	-	0.25	15
5	MWNT	20	3.7	-	2.6	-	0.1	420	637	-	0.83	-	16
6	AC	1472	13	0.4	1.2	0.4	10	400	30000[c]	15.2	-	-	17
7	NCs	-	1.0	-	-	4.3	1	400	60000[d]	-	32.9	0.007	18
8	HSGC	346	4.0	-	2.6	0.7	10	400	10000	15.6	-	0.10	19
9	AC[e]	522	4.3	-	-	1.0	1	400	36000[d]	-	38.0	-	20
10	MPC	430	6.7	2.5	-	-	1	400	9000	3.4	68.0	0.062	21
11	AC	-	4.8	-	23[f]	1.0	1	400	-	-	19.6	0.28	22
12	SGCNT	430	10	2.5	-	-	5	400	7000	14.6	-	0.038	23

[a] Mesoporous carbon plate (MCP), carbon-covered alumina (CCA), activated carbon (AC), multiwalled nanotube (MWNT), N-doped carbon spheres (NCs), high-surface-area graphitic carbon (HSGC), carbon nanofiber (CNF), and mesoporous carbon material (MPC).
[b] H$_2$/N$_2$ molar ratio = 3
[c] H$_2$/N$_2$ molar ratio = 1.5
[d] WHSV with units of mL g^{-1} h^{-1}
[e] Treated with gas-phase nitric acid
[f] Ru/AC catalyst with dual Li and Ba promoters and a Li/Ru molar ratio of 23.

ammonia synthesis rate and the potential methanation-induced catalyst deactivation. Temperature-programmed methods and in situ spectroscopic techniques were employed to clarify the formation of active components during reductive activation and their function under catalytic conditions as well as the spillover-hydrogen-induced methane production above 500 ºC. The optimal catalyst was a Cs-promoted Ru catalyst supported on the prepared carbon support with high graphitization degree with 10 wt% of Ru and Cs/Ru molar ratio of 2.5, behaving high ammonia synthesis activity below methanation temperature. It was further studied for pressured and intermittent ammonia synthesis and subjected to kinetic analyses. Density functional theory (DFT) calculations were performed to elucidate the adsorption of hydrogen on the Ru surface to understand how the hydrogen species could poison the active sites intended for mild ammonia synthesis. Both hydrogen poisoning and spillover-hydrogen-induced methane production can be reduced by adding CsOH to the Ru catalysts as evidenced by the obtained experimental and DFT-derived data.

2. Experimental section

2.1. Synthesis of SBA-15 plates

Santa Barbara Amorphous (SBA-15)-type mesoporous silica plates (denoted as p-SBA-15) were synthesized using a modified version of previously reported procedures [32–34]. The synthesis solution was prepared by completely dissolving zirconium oxychloride (ZrOCl$_2$•8 H$_2$O, 1.31 g; Acros) and Pluronic P123 triblock copolymer (8.04 g, Aldrich) in HCl (294 mL, 1.6 M) at 35 °C. The resulting solution was mixed with tetraethyl orthosilicate (TEOS, 1.70 g; Acros) and then stirred at 35 °C for 30 min. The molar composition of the synthesis mixture (TEOS/ZrOCl$_2$•8 H$_2$O/HCl/P123/H$_2$O) was 1:0.05:5.9:0.017:193. The mixture was incubated at 35 °C for 24 h and then aged at 90 °C for 24 h. Subsequently, concentric sulfuric acid (97.0%, 23.2 g; Showa) was added dropwise, and the resulting mixture was stirred at 90 °C for another 24 h. The obtained solution was then neutralized with a 0.5 M ammonia solution, and a white solid was obtained after subjecting the synthesis gel to vacuum filtration. The solid was successively washed with deionized water (~800 mL) and acetone (~100 mL) and then dried at 90 °C for 8 h. The resulting solid was heated at 350 °C for 6 h at a rate of 5 °C min^{-1} to completely decompose and remove the organic residuals.

2.2. Preparation of mesoporous carbon plates

MCPs were fabricated using previously reported procedures with modifications [34–36]. Furfuryl alcohol and p-SBA-15 were used as the carbon source and hard template, respectively. Briefly, dried p-SBA-15 (1.00 g) was impregnated with a precursor solution containing oxalic acid (0.76 g, Fluka) and furfuryl alcohol (1.525 mL, Aldrich). The mixture was heated at 105 °C for 12 h to enable polymerization of furfuryl alcohol. The polymerized species in the mixture were dehydrated and partially decomposed in a nitrogen atmosphere by heating at 80 °C for 2 h at a rate of 5 °C min^{-1}, followed by further heating at 350 °C for 4 h at a rate of 5 °C min^{-1}. After cooling to room temperature, the sample was again impregnated with a precursor solution containing oxalic acid (0.01 g) and furfuryl alcohol (0.022 mL), followed by heating at 105 °C for 6 h. Subsequently, carbonization was conducted in a nitrogen atmosphere by heating at 350 °C for 4 h at a rate of 5 °C min^{-1} and then at the designated temperature (600, 850, or 1100 °C) for 4 h at a rate of 5 °C min^{-1}. The silica template in the resulting samples was finally removed by stirring each sample (1.00 g) in a 5% aqueous HF solution (200 mL) for 30 min. To ensure complete silica removal, the solution was decanted and the 5% HF solution (200 mL) was added again to allow the solid to react further for 30 min. Finally, a black solid was collected by vacuum filtration, washed sequentially with deionized water (~100 mL) and ethanol (~100 mL), and then dried at 90 °C for 8

h. The fabricated MCP samples are designated as MCP-*x*, where *x* denotes the carbonization temperature (600, 850, and 1100 °C).

2.3. Preparation of MCP-supported Ru catalysts

MCP-supported Ru catalysts were prepared using a wet impregnation method. Briefly, Ru precursor solutions were prepared by dissolving the Ru precursor nitrosylruthenium(III) nitrate (Ru(NO)(NO$_3$)$_3$; 0.03–0.35 g) in a 50% (v/v) water–ethanol solution (0.56–0.68 mL). Under ambient conditions, each MCP-*x* sample (1.0 g) was impregnated with the Ru precursor solution whose volume was 1.1 times the total pore volume of the MCP-*x* sample. The impregnated sample was heated at 70 °C overnight to completely evaporate the solvent. Subsequently, the sample was heated under nitrogen flow (50 mL min^{-1}) at 400 °C for 3 h at a rate of 5 °C min^{-1} to reduce the metal through thermal decomposition [21,23,55], cooled to room temperature, and then exposed to air for 1 h to passivate the metal NPs. The resulting samples with 1–10 wt% Ru loading are designated as *y*Ru/MCP-*x*, where *y* denotes the Ru loading (wt%; *y* = 1, 5, or 10).

Cs-loaded Ru catalysts were also prepared via wet impregnation. Each *y*Ru/MCP-*x* sample (1.0 g) was dispersed in a water–ethanol solution (50%, v/v; 50 mL) containing cesium carbonate (Cs$_2$CO$_3$, 0.08–0.48 g; Alfa Aesar). The mixture was slowly heated at ~50 °C under vacuum until the solvent evaporated completely. The resulting samples are designated as *z*Cs-*y*Ru/MCP-*x*, where *z* denotes the Cs/Ru atomic ratio (Cs/Ru = 0.5, 1.0, 2.5, or 3.0).

2.4. Catalyst characterization

Powder X-ray diffractometry (PXRD) patterns were recorded using a Brucker D8 Advance diffractometer with Cu Kα radiation. Nitrogen physisorption isotherms were obtained at 77 K using a Micromeritics TriStar II Plus instrument, with each sample evacuated at 150 °C for 12 h prior to the measurements. The Brunauer–Emmett–Teller (BET) surface area was calculated from the adsorption branch in the relative pressure range 0.05–0.30, and the total pore volume was evaluated at a relative pressure of 0.95. The average pore diameter and pore size distribution were calculated from the desorption branch using the Barrett–Joyner–Halenda (BJH) method. Transmission electron microscopy (TEM) images were obtained using a JEOL JEM-2100 microscope operating at 200 kV. High-resolution images were obtained by scanning transmission electron microscopy (STEM) using a JEOL JEM-ARM200FTH microscope operating at 200 kV and equipped with an energy-dispersive X-ray spectrometer (EDS, Ultim Max). Field-emission scanning electron microscopy (FE-SEM) images were acquired using a Hitachi Regulus 8230 microscope operating at 1 kV and 15 mA, equipped with an EDS (Ultim Extreme) for quantitative analysis. Analysis of X-ray fluorescence spectroscopy (XRF) was conducted using a Rigaku NEX DE spectrometer. Raman spectra were obtained using a Horiba XplotRa ONE microscope with a 532-nm Nd:YAG laser as the excitation source. Elemental analysis was conducted using an Elementar Vario EL cube analyzer, and the metal content was determined by inductively-coupled-plasma mass spectroscopy (ICP-MS; Agilent 7500ce). Thermogravimetric analysis (TGA) was conducted in air or H$_2$ (denoted as air-TGA and H$_2$-TGA, respectively), with air-TGA data obtained using a Mettler-Toledo TGA/DSC 2-HT instrument. To that end, ~10 mg of each sample was loaded into an alumina crucible and purged with airflow (35 mL min^{-1}) for 10 min before being heated to 800 °C at a rate of 10 °C min^{-1}. For the H$_2$-TGA measurements (Rigaku TG-DTA8122), a dried sample (~5 mg) was loaded into an alumina crucible and purged with 5 vol% H$_2$ flow (diluted with Ar, 100 mL min^{-1}) for more than 30 min prior to being heated to 800 °C at a rate of 5 °C min^{-1} under H$_2$ flow (30 mL min^{-1}). CO pulse chemisorption was performed using a BELMETAL-3 instrument. Prior to the measurements, the samples were reduced at 350 °C for 2 h under H$_2$ flow (50 mL min^{-1}), followed by cooling to 50 °C under He flow (50 mL min^{-1}). For the CO pulse

chemisorption experiments, a sequential pulse of CO gas was injected into the reduced sample chamber using a standard gas—5 vol% CO/He—until no more CO was adsorbed; this was monitored by thermal conductivity detection (TCD).

2.5. In situ measurements using synchrotron X-ray sources

2.5.1. X-ray absorption spectroscopy (XAS)

XAS measurements at the Ru K-edge and Cs L_3-edge were conducted in transmission mode using the TLS 01 C and TLS 17 C beamlines, respectively, at the National Synchrotron Radiation Research Center (NSRRC, Taiwan) with a storage ring energy of 1.50 GeV and an electron beam current of 360 mA in the top-up injection mode. The photon flux was guided using a Si(111) monochromator, and the photon energy was calibrated using foils of Ru (for the Ru K-edge) or Ti (for the Cs L_3-edge). For the measurements, the catalyst was packed into an in situ cell with a Kapton window and heated at 350 °C under hydrogen flow (50 mL min^{-1}) for 2 h. After the cell was cooled to room temperature, X-ray absorption near-edge structure (XANES) and extended X-ray absorption fine structure (EXAFS) spectra were recorded. Multiple scans were performed and averaged to enhance the signal-to-noise ratio. Certain samples were also assessed prior to the hydrogen reduction step and the sample will be named with -R afterward. For example, 2.5Cs-10Ru/MCP-1100-R represents that 2.5Cs-10Ru/MCP-1100 was reduced at 350 °C for 2 h under H$_2$ flow. The collected spectra were analyzed using ATHENA and ARTEMIS programs. The sizes of the metallic hexagonal-close-packed Ru particles in the samples were estimated from the fitted coordination number (CN) using a Hill function, assuming a hemispherical shape for the nanoparticles [37].

2.5.2. Near-ambient-pressure X-ray photoelectron spectroscopy (NAP-XPS)

NAP-XPS measurements were conducted using the wide-range beamline (TLS BL24A) at NSRRC. The end station comprised a load lock chamber for sample loading, an ultrahigh-vacuum chamber for sample preparation, and a main analysis chamber for electron spectroscopy measurements under ambient pressure, which were performed using a SPECS NAP 150 electron energy analyzer; details concerning the end station have been reported elsewhere [38]. An X-ray with photon energy of 980 eV impinged on a pelletized MCP-supported sample at an angle of 55° from the sample normal and projected an elongated footprint of 1.1 mm × 0.3 mm. XPS profiles of the sample being evacuated at 25 °C were first acquired. Subsequently, hydrogen (2 mbar) was introduced into the analysis chamber, and the sample was heated at 350 °C for 20 min at a rate of 5 °C min^{-1}. XPS profiles of the reduced samples were also acquired after they cooled to 25 °C with background hydrogen gas at a pressure of 0.2 mbar. The binding energies of all spectra were calibrated to an internal reference—the Au 4 f$_{7/2}$ photoemission peak of a gold mesh at 84.0 eV.

2.6. Temperature-programmed analyses

2.6.1. Temperature-programmed reduction (TPR) study of reductive activation

Reductive activation of the prepared samples was monitored by TPR analysis performed under 5%H$_2$/Ar gas flow with quadrupole mass spectrometry (H$_2$-TPR-MS). The H$_2$-TPR-MS profiles were acquired in the temperature range from − 50 to 800 °C using a BELCATII instrument with a BELMASS mass spectrometer. Prior to the measurements, dried samples were packed in a quartz tube and sandwiched between quartz wood panels. This sample-assembling system was integrated into the instrument and then purged with Ar flow at − 50 °C for 30 min and subsequently with 5%H$_2$/Ar flow until the baseline was stable, as monitored by TCD and MS.

2.6.2. Temperature-programmed surface reaction (TPSR) analysis of ambient-pressure ammonia synthesis activity

The ammonia synthesis activity of the prepared catalysts was surveyed in the temperature range of 50–800 °C by TPSR analysis using procedures similar to those described in Section 2.6.1. Prior to the measurements, dried samples were reduced at 350 °C for 2 h under H$_2$ flow, purged with Ar flow and cooled to ~50 °C for 30 min, and then purged with a H$_2$/N$_2$ gas mixture (H$_2$/N$_2$ molar ratio = 3) until the baseline was stable, as monitored by TCD and MS. Details of the analysis of MS signals for TPSR experiments is given in ESI.

2.6.3. Temperature-programmed desorption (TPD) analysis of species adsorbed on active components

The species adsorbed on the active components of the prepared catalysts participating in reductive activation at 350 °C with H$_2$ gas and ammonia synthesis at 400 °C with a H$_2$/N$_2$ gas mixture (H$_2$/N$_2$ molar ratio = 3) were monitored by TPD analysis using procedures similar to those described in Section 2.6.2. Specifically, the H$_2$, N$_2$, and NH$_x$ species were quantitatively analyzed and correlated with experimental data, particularly those obtained via the in situ studies, kinetics and catalytic behavior analyses, and DFT calculations.

2.7. Pressurized ammonia synthesis

The ammonia synthesis activity of the prepared 2.5Cs-10Ru/MCP catalyst was determined twice using a fixed-bed stainless-steel reaction system connected to an online Shimadzu GC2014 gas chromatography (GC) instrument. A quartz inlet was incorporated into the fixed-bed stainless-steel reactor. A dried catalyst (0.20 g, approximately 1.2 cm^3) was packed in the quartz tube, which was then sandwiched between quartz wood panels and integrated with the fixed-bed stainless-steel reaction system. Prior to the reaction, the catalysts were reduced at 350 °C for 2 h under H$_2$ flow and spontaneously cooled to 200 °C under mixed H$_2$/N$_2$ gas flow (H$_2$/N$_2$ molar ratio = 3) at ambient pressure (0.1 MPaG). In a typical reaction (WHSV: 6600 mL g^{-1} h^{-1}), the pressure was increased to 0.9 MPaG, and the temperature was increased from 200 to 600 °C. At specific reaction temperatures, the NH$_3$ yield in the downstream unit was analyzed in situ using the GC instrument equipped with a Thermon-3000 + KOH (2 + 2)% Sunpak-N 60/100 mesh column (length, 2.1 m; internal diameter, 3.2 mm; Shinwa Chemical Industries, Japan) and the TCD device.

2.8. Kinetic analysis of ammonia synthesis

The reaction orders of ammonia synthesis over the 2.5Cs-10Ru/MCP-1100 catalyst were studied using a fixed-bed reactor at 380 °C and 0.9 MPa by following previously reported procedures [23]. In Eq. (1), the ammonia synthesis rate r is related to the partial pressures of N$_2$, H$_2$, and NH$_3$ through their respective reaction orders—n, h, and a. Details concerning these measurements and calculations are provided in Table S2. To minimize the influence of the reverse reaction, conditions were employed to ensure that the outlet ammonia concentration was less than 30% that at thermodynamic equilibrium.

$$r = k_1 P_{N2}^n P_{H2}^h P_{NH3}^a \tag{1}$$

2.9. DFT calculations

Spin-polarized DFT calculations were performed using Vienna Ab initio Simulation Package (VASP) [39,40]. Projector-augmented-wave (PAW) pseudopotentials and Perdew–Burke–Ernzerhof (PBE) functionals were adopted [41,42]. Dispersion correction was performed using the DFT-D3 method with a zero-damping function [43,44]. To probe the hydrogen spillover onto the Cs-promoted Ru/MCP-x catalysts, three models were constructed using single-vacancy graphene (SVG) as the supporting material, which excluded the effects of the morphology

and interaction of Ru particles with the carbon support. Thus, three models of a single Ru atom on SVG without and with promoters (Cs or CsOH) were constructed: Model (I)—denoted as Ru/SVG—comprises a Ru atom bound to the C–C–C hollow site with no Cs promotion effect (Fig. S23). Model (II)—designated as Ru–Cs/SVG—comprises a Ru atom bound to a metallic Cs^0 atom (Fig. S23). Model (III)—denoted as Ru–CsOH/SVG—involves a Ru atom bound to a CsOH species (Fig. S23). The activation energy of hydrogen spilled over from the Ru atom to the SVG support (Model I) was compared with those of Models II and III. The models were bound to a 6 × 6 supercell of the SVG with dimensions a = 14.81 Å, b = 14.81 Å, and c = 20 Å. The calculations were performed at a plane-wave cutoff energy of 450 eV with a 2 × 2 × 1 k-mesh. The conjugate gradient algorithm was implemented for geometry optimization until the forces upon each atom were smaller than 0.01 eV Å^{-1}, and the energy convergence was performed up to 10^{-5} eV [45]. Multiple hydrogen adsorption energies (E_{ads}) of the three models (Ru/SVG, Ru–Cs/SVG, and Ru–CsOH/SVG) were calculated using the equation $E_{ads} = E_{tot} - E_{bare} - n \times 0.5 \times E_{H2}$, where E_{tot} represents the total energy of hydrogen adsorption on the models, E_{bare} denotes the total energy of the bare models, n symbolizes the number of H$_2$ molecules adsorbed, and E_{H2} is the total energy of the H$_2$ molecules. The energy barriers of hydrogen spilled over from Ru to SVG in the three models were calculated using the climbing-image nudged elastic band (CI-NEB) method [46]. The force convergence of the intermediate images was optimized up to 0.01 eV Å^{-1}.

3. Results and discussion

3.1. Characterization of mesoporous carbon plates

MCPs were fabricated using mesoporous silica p-SBA-15 as the hard template. p-SBA-15 exhibited an ordered hexagonal mesostructure (with *p6mm* symmetry) and showed 10, 11, and 20 reflections in its small-angle PXRD pattern (Fig. S1). The calcined sample retained these mesostructural features and exhibited a type IV nitrogen physisorption isotherm with a sharp step and an H$_1$-type hysteresis loop; this corresponds to the filling of uniform mesopores with an open cylindrical geometry. The unit cell parameter derived from the PXRD pattern and the mesopore diameter estimated from the nitrogen physisorption isotherm were 11.2 and 8.5 nm, respectively. FE-SEM imaging revealed the plate morphology of the particles in the sample as well as the average width—defined as the edge-to-edge distance—and thickness (~900 nm and ~300 nm, respectively). The ordered arrangement of the channel-type mesopores in p-SBA-15 was directly observed by TEM.

Using the calcined p-SBA-15 as the hard template, MCPs were prepared by carbonization of the infiltrated poly(furfuryl alcohol) (PFA) in a nitrogen atmosphere at 600, 850, and 1100 °C. Small-angle PXRD revealed that the three MCP samples retained the ordered mesostructure of p-SBA-15 with varying degrees of shrinkage (Fig. 1a). The derived unit cell parameters for MCP-600, MCP-850, and MCP-1100 were 11.2, 11.0, and 10.7 nm, respectively. Additionally, the nitrogen physisorption isotherms of the MCPs (Fig. 1b) showed a step at a relative pressure of ~0.4, suggesting the existence of pore size distributions centered at 3.4–3.5 nm. The evaluated textural properties of the MCP samples are listed in Table S3. Elemental analysis indicated that the three samples contained 90–95 wt% carbon, ~3–4 wt% hydrogen, and 2–5 wt% oxygen (Table S3). The amounts of hydrogen and oxygen decreased with increasing MCP carbonization temperature. Moreover, Si was not detected by EDS (< 0.1 wt%) and XRF (not detectable) in any of the three samples, suggesting that the hard template was completely dissolved and removed. Air-TGA data revealed weight losses of 100% for the three samples at temperatures higher than 600 °C (Fig. 1c), with
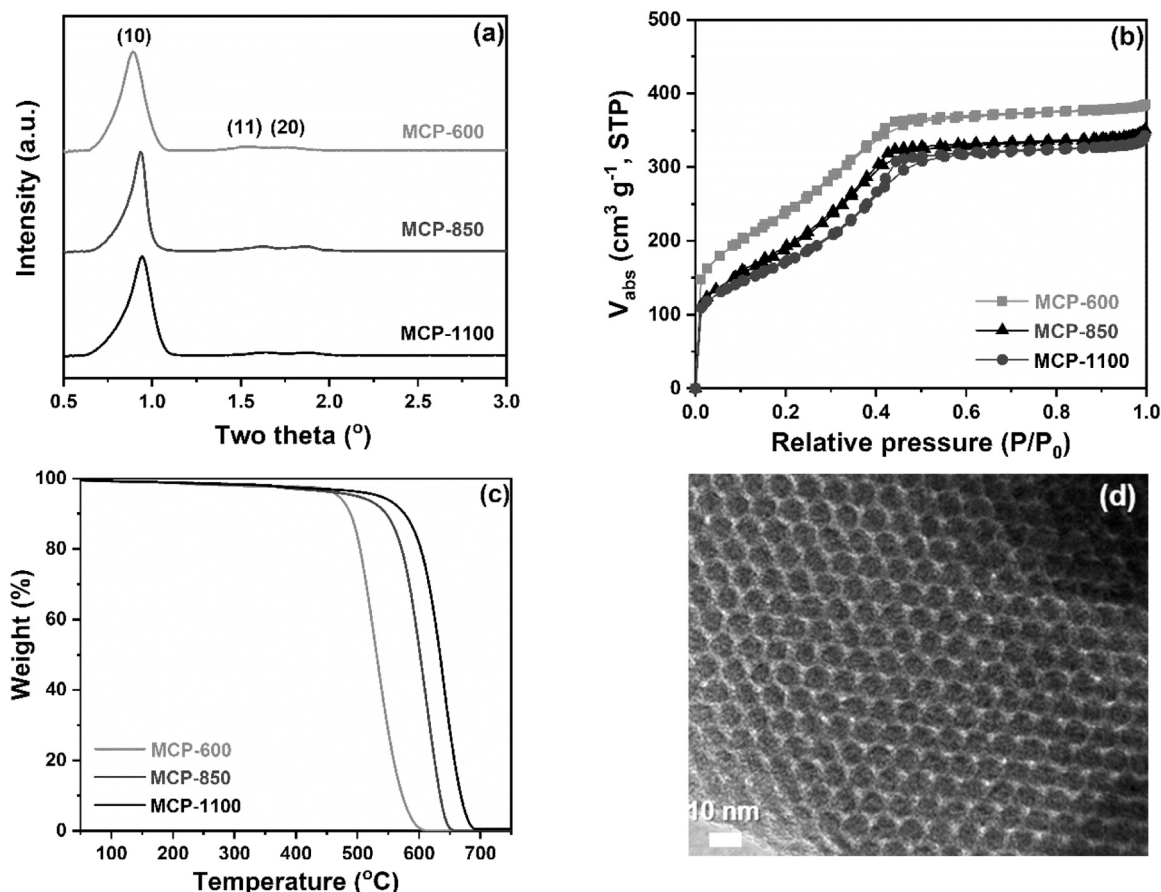

Fig. 1. (a) Small-angle PXRD patterns, (b) N$_2$ physisorption isotherms, and (c) air-TGA profiles of MCP-600, MCP-850, and MCP-1100. (d) TEM image of MCP-1100.

oxidative decomposition initiated at ~470, ~500, and ~520 °C for MCP-600, MCP-850, and MCP-1100, respectively. The positive correlation between the decomposition temperature and carbonization temperature was due to the structure of the MCP materials. All three samples exhibited two broad peaks in their wide-angle PXRD patterns in the considered two-theta range (Fig. S2); these were probably associated with the (002) and (100) reflections of the graphitic structure of the carbon materials [47,48]. The (002) peak of MCP-600, which was centered at 22.0°, increased in intensity and shifted to 23.4° for MCP-850 and 23.9° for MCP-1100. This suggested that the graphitization degree of the MCP materials increased with increasing carbonization temperature [47,48]. The FE-SEM (Fig. S3) and TEM images (Fig. 1d and S4) further confirmed the replication of both the ordered mesostructure and the overall particle morphology of p-SBA-15, which yielded plate-shaped mesoporous carbon materials comprising hexagonally arranged carbon nanorods.

The MCP-x materials were further analyzed by Raman spectroscopy—a powerful tool for characterizing carbon-based materials, which is sensitive to structural defects in bulk-scale samples. Raman spectra obtained using an excitation wavelength of 532 nm and their deconvolutions were assessed (Fig. 2). Based on a previous report on porous carbon materials derived from PFA [49], the Raman spectra were deconvoluted using the Levenberg–Marquardt algorithm into six Lorentzian-shaped bands (G, D, D', A_1, A_2, and S). The spectra were adequately fit, and the positions and relative intensities of each band for the three samples were examined (Table 2). The "defect" (D) band at ~1350 cm^{-1} and the "graphite" (G) band at ~1580–1600 cm^{-1} were the noteworthy features; these are typically assigned to K-point phonons with A_{1g} symmetry and zone-center phonons with E_{2g} symmetry, respectively [49–52]. The D and D' bands at ~1620 cm^{-1}, which correspond to the double-resonance-activated breathing mode, are characteristic of disordered graphite [49–52]. In terms of the mechanism underlying the thermal decomposition of PFA in an inert atmosphere [53], the oxygen-containing groups of PFA start decomposing to form condensed aromatic species at ~400 °C, and the partially decomposed polymer chains and polyaromatic domains continue to transform into graphite-like species as the temperature is further increased. Ferrari *et al.* [50] interpreted the Raman spectra of disordered and amorphous carbon and presented a phenomenological three-stage model relating the Raman parameters—primarily the G and D peaks—to the sp^2 nanostructure and disordered carbon content. They defined an amorphization trajectory from graphite to nanocrystalline graphite (*nc*-G), amorphous carbon (*a*-C) with a considerably low C–C sp^3 content, and finally to tetrahedral amorphous carbon (*ta*-C) with a higher sp^3 content [50]. For the MCP materials carbonized at 600–1100 °C, the structural transformation of the carbonaceous species may be correlated to the second stage of the model, that is, in between *a*-C and *nc*-G. At this stage, the main effects on the evolution of the Raman spectrum include the G band position shifting from ~1510 to 1600 cm^{-1} and the intensity ratio of the D and G bands (I_D/I_G) increasing with increasing sp^2/sp^3

ratio [50]. Notably, these trends were exhibited by the MCP materials, in that the G band position shifted from 1582 cm^{-1} for MCP-600 to 1591 and 1593 cm^{-1} for MCP-850 and MCP-1100, respectively, and I_D/I_G increased from 1.17 for MCP-600 to 1.43 and 1.67 for MCP-850 and MCP-1100, respectively. The observed trends indicate that the sp^2/sp^3 ratio, or degree of graphitization, of the MCP materials increased with increasing carbonization temperature.

Furthermore, the other three bands—S, A_1, and A_2—provided additional information on the microstructure and composition of the MCP materials. The "shoulder" (S) band is mainly assigned to the breathing modes of cyclic systems containing seven-membered rings and the benzene rings adjacent to heteroatom defects [52]. Generally, the band position shifts toward a lower frequency and the relative intensity decreases with increasing carbonization temperature. For MCP-850 and MCP-1100, the band position fell within the S-band range of ~1150–1200 cm^{-1}. However, for MCP-600, the band position was slightly farther away (1240 cm^{-1}) and lay between the spectral ranges of the S and D_s bands (1250–1300 cm^{-1}); this can be assigned to the breathing modes of small polyaromatic hydrocarbons (PAHs) [52]. Because small PAHs can form during the pyrolysis of PFA at temperatures above 400 °C [53], the evolutions of the position and relative intensity of the S-band of the MCP materials suggest the existence of small PAHs in MCP-600 and their further dehydrogenation and transformation into larger PAHs with increasing carbonization temperature. However, the "amorphous" (A) bands between the D and G bands are generally believed to be related to irregular structures [49–52]. Although uncertainty remains in the assignment of these bands, the A_1 band (1400–1460 cm^{-1}) is ascribed primarily to Kekulé -dominated vibrations coupled to the symmetric breathing of an adjacent cyclopentane ring, and the A_2 band (1480–1550 cm^{-1}) is attributed to a mixture of breathing and asymmetric stretching modes of ring systems adjacent to point defects or heteroatom defects [52]. Slight changes were observed in the positions and relative intensities of both bands for the three samples. Special attention was paid to the relationship between the frequency shift of the A_2 band and the density of heteroatom defects in the MCP materials. The defects, especially those of oxygen, partially restrict the integration of the asymmetric stretching modes and breathing modes, resulting in a strong red shift toward 1480 cm^{-1} [52]. A lower carbonization temperature yielded an MCP material with a lower A_2-band frequency; this appears to correlate well with the results of elemental analysis (Table S3), which indicated that MCP-600 had a higher amount of oxygen (~5.2%) than that in MCP-850 (~3.3%) and MCP-1100 (~2.3%).

3.2. Characterization and catalytic studies of Ru/MCP

3.2.1. Effect of carbonization temperature on 10Ru/MCP-x performance

A set of Ru/MCP-x samples was prepared using the three carbon supports with identical Ru loadings (10 wt%) by wet impregnation of nitrosylruthenium(III) nitrate, followed by heat treatment at 400 °C
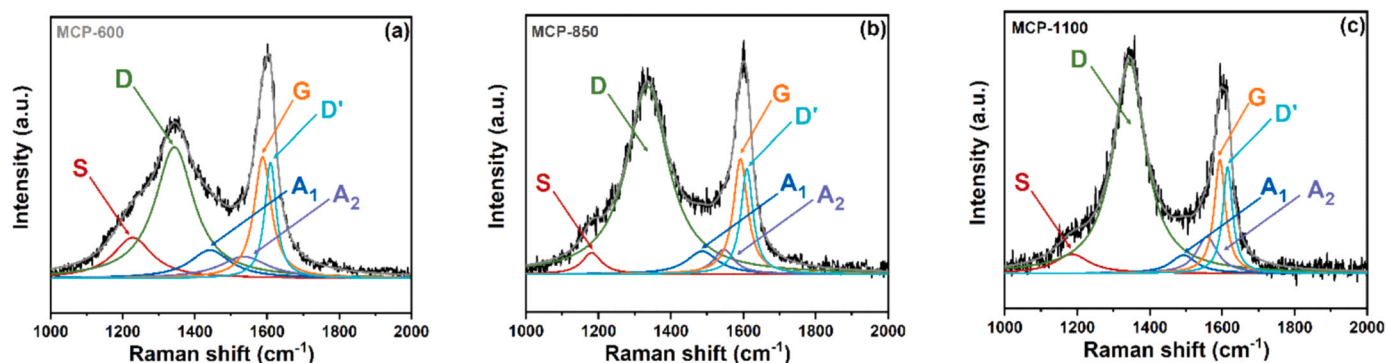

**Fig. 2.** Raman spectra and deconvoluted bands of MCP-x materials.

Table 2
Positions and relative intensities of deconvoluted peaks in the Raman spectra of MCP-*x* materials.

Sample	S-band		D band		A$_1$ band		A$_2$ band		G band		D' band	
	n (cm^{-1})	I (arb. units)	n (cm^{-1})	I (arb. units)	n (cm^{-1})	I (arb. units)	n (cm^{-1})	I (arb. units)	n (cm^{-1})	I (arb. units)	n (cm^{-1})	I (arb. units)
MCP-600	1240	0.37	1342	1.08	1430	0.28	1521	0.23	1582	1	1608	0.96
MCP-850	1187	0.23	1336	1.60	1483	0.24	1550	0.26	1591	1	1612	0.92
MCP-1100	1184	0.15	1344	1.87	1504	0.15	1562	0.31	1593	1	1615	0.94

under nitrogen flow and passivation at room temperature in air. The metal loadings of the three samples determined via elemental analysis and ICP-MS (9.3–9.6 wt%) were close to the nominal value of 10 wt%. In the small- and wide-angle PXRD patterns of the resulting 10Ru/MCP-*x* samples (Fig. 3a and b, respectively), the ordered mesostructure of the carbon supports was preserved during metal loading, and the unit cell parameters derived from the small-angle PXRD patterns were almost identical to those of MCP-*x*. However, additional reflections attributed to surface passivated Ru NPs were not apparent in the wide-angle PXRD patterns of the samples, indicating that the NPs had to be extremely small. The three samples were also subjected to nitrogen physisorption analysis (Fig. 3c). For a fair comparison, the isotherms were normalized to the weight of the MCP support instead of the total sample weight, because the metal loading of the samples differed slightly. The isotherms were remarkably similar in shape to those of the corresponding MCP-*x* supports (Fig. 1b), with the step also appearing at a relative pressure of

~0.4. The as-determined textural properties of 10Ru/MCP-*x* are listed in Table 3. Because the 10Ru/MCP-*x* samples exhibited pore diameters that were almost identical to those of MCP-*x*, and their total pore volumes (per gram of MCP support) were significantly smaller than those of MCP-*x*, the Ru NPs were mainly located in the mesopores among the hexagonally arranged carbon nanorods. This was confirmed by TEM images (Fig. S5), which revealed the high dispersion of uniformly sized Ru NPs (~2.2–2.5 nm, Table 3) in the channels of the MCP-*x* supports. The FE-SEM image of the ruptured plates in 10Ru/MCP-1100 (Fig. 3d) clearly showed well-aligned basalt-like microstructures of carbon with numerous miniscule nanoparticles—most likely Ru—in the channel-like pores. The size and dispersion of Ru NPs in these samples were further studied using the pulsed CO chemisorption method. The Ru NP dispersion calculated from CO uptake was 47–53% (Table 3), indicating the presence of 2.5–2.8-nm-sized metal NPs in the samples under the assumption of spherical geometry. The estimated particle sizes are
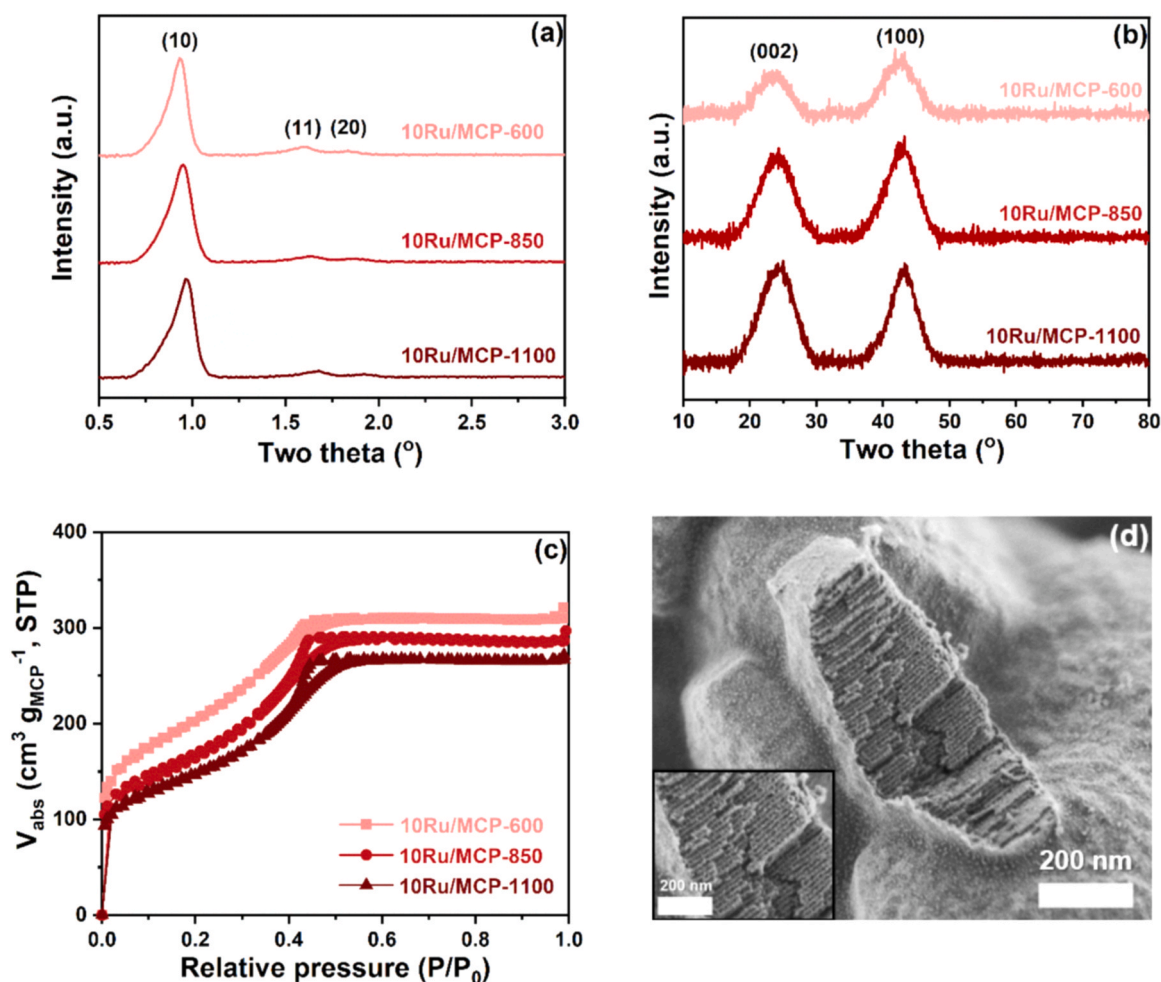
Fig. 3. (a) Small-angle PXRD patterns, (b) wide-angle PXRD patterns, and (c) N$_2$ physisorption isotherms of 10Ru/MCP-*x* samples. (d) FE-SEM image of 10Ru/MCP-1100.

Table 3

Textural properties and elemental analysis of 10Ru/MCP-*x* materials[a].

Sample	S_{BET} (m^2 g$_{MCP}^{-1}$)	V_t (mL g$_{MCP}^{-1}$)	D_P (nm)	CO chemisorption			TEM imaging
				Uptake (cm^3 g^{-1})	Dispersion (%)	Ru size (nm)	Ru size (nm)
10Ru/MCP-600	754	0.50	3.5	11 ± 3.3	52 ± 14	2.8 ± 1.0	2.2 ± 0.4
10Ru/MCP-850	612	0.46	3.5	10 ± 0.8	47 ± 3.6	2.8 ± 0.2	2.3 ± 0.5
10Ru/MCP-1100	545	0.43	3.5	11 ± 0.9	53 ± 3.9	2.5 ± 0.2	2.5 ± 0.4

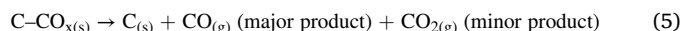[a] S_{BET}: BET surface area; V_t: total pore volume determined at P/P$_0$ = 0.95; D: average pore diameter.

consistent with the TEM analysis results.

Reductive activation of the 10Ru/MCP-*x* samples was studied by H$_2$-TGA and H$_2$-TPR-MS, in which the H$_2$, CH$_4$, CO, and CO$_2$ signals were recorded using a BELMASS mass analyzer at *m/z* ratios of 2, 16, 28, and 44, respectively. The H$_2$-TGA and H$_2$-TPR-MS results indicated that the reductive activation of the 10Ru/MCP-*x* samples could be divided into two parts: (i) reduction of RuO$_2$ to Ru at ~100 °C (Fig. 4, S6, and S7), accompanied by the formation of H$_2$O (Fig. S8) and removal of CO$_2$ predominantly derived from the atmosphere (Fig. 4d; Eqs. 2 and 3), and (ii) methanation of CO$_2$ at temperatures above 200 °C (Eq. 4) and thermal decomposition of the carbon framework at temperatures above 450 °C (Eq. 5) (Fig. 4b and S7).

Part (i): (temperature ≈ 100 °C).

$$RuO_{2(s)} + 2\,H_2 \rightarrow Ru_{(s)} + 2\,H_2O_{(g)} \tag{2}$$

$$*\text{–}CO_2 \rightarrow * + CO_{2(g)} \tag{3}$$

Part (ii): (temperature > 200 °C).

$$C_{(s)} + *\text{–}H \rightarrow * + CH_{4(g)} \tag{4}$$

$$C\text{–}CO_{x(s)} \rightarrow C_{(s)} + CO_{(g)} \text{ (major product)} + CO_{2(g)} \text{ (minor product)} \tag{5}$$

In Part (i), the reduction temperature of 10Ru/MCP-*x* ($T_R \approx 100$ °C) was lower than that of bulk RuO$_2$ ($T_R \approx 170$ °C), indicating the presence of Ru nanoparticles. The corresponding H$_2$-TGA profiles showed weight losses of 2.6–3.4 wt%, which was similar to the nominal amount of RuO$_2$ reduced by H$_2$ to form metallic Ru (weight loss: ~3.27 wt%). The H$_2$/Ru molar ratio (~2) obtained from the H$_2$ consumption analysis indicated that RuO$_2$ particles could be completely reduced to metallic Ru because of the weak Ru–carbon material interactions. This finding differs from that of our recent study on the reduction of the Ru/γ-Al$_2$O$_3$ catalyst, in which RuO$_2$ was reduced at $T_R \approx 150$ °C and H$_2$/Ru molar ratio < 2, which led to incomplete reduction of RuO$_2$ at the Ru/γ-Al$_2$O$_3$ interface [54]. Notably, a minimal amount of CO$_2$ derived from the atmosphere
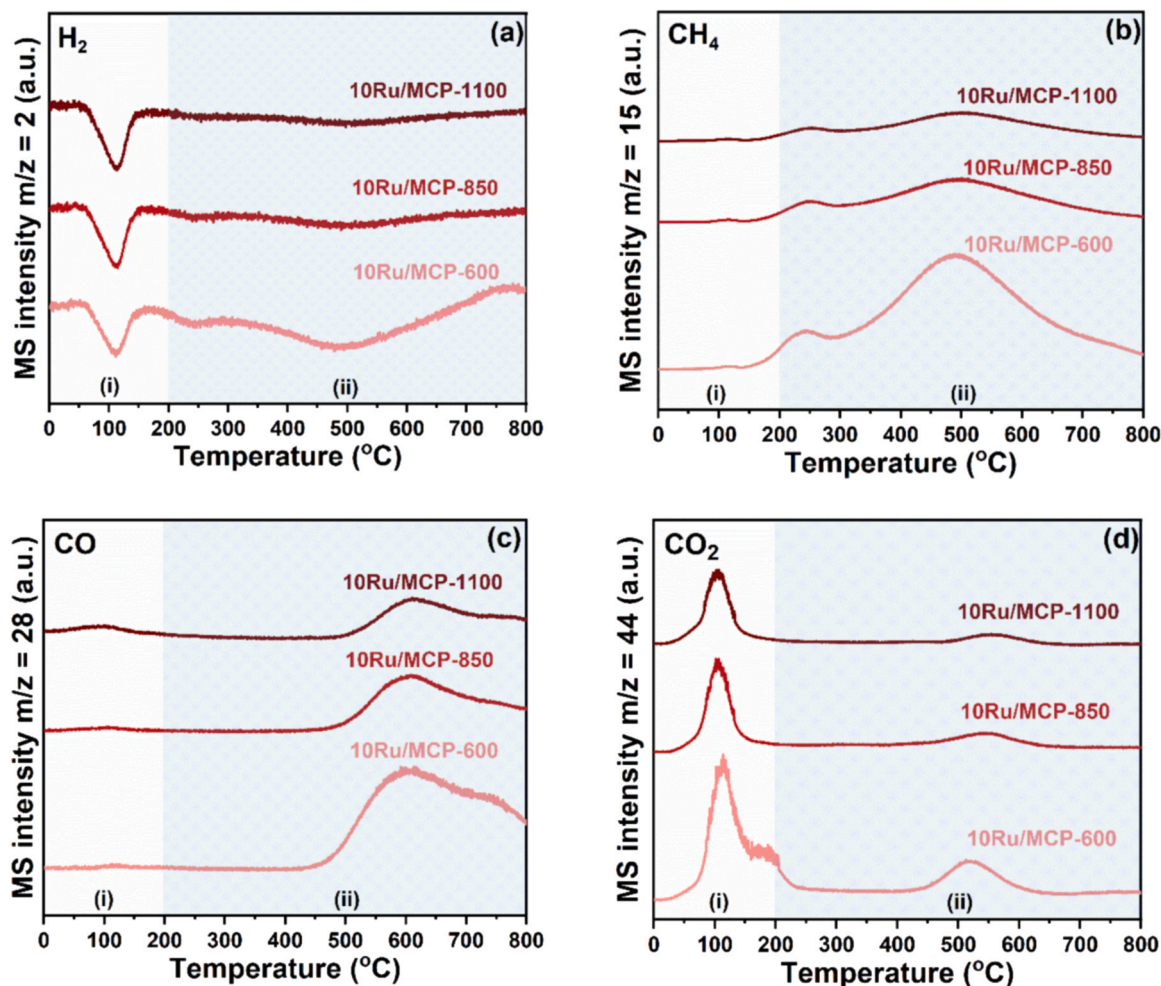
Fig. 4. H$_2$-TPR-MS profiles of 10Ru/MCP-650, 10Ru/MCP-850, and 10Ru/MCP-1100 monitored by *m/z* ratios of 2, 15, 28 and 44 for (a) H$_2$, (b) CH$_4$, (c) CO, and (d) CO$_2$.

was detected at 50–250 °C (Fig. 4d). A portion of this was probably reduced by the spilled-over H_2 to form CH_4, particularly in the case of 10Ru/MCP-600; this observation is consistent with our previous study [54].

In Part (ii), methanation of the carbon framework with hydrogen spilled over from Ru particles was observed at temperatures above 300 °C. The methane signal for 10Ru/MCP-600, which had a relatively high surface area and low graphitization degree, was considerably stronger than those of 10Ru/MCP-850 and 10Ru/MCP-1100, which had a relatively low surface area and high graphitization degree. This indicated that the carbon framework of MCP-600 was unstable under hydrogen-rich conditions. Similar results were obtained for the thermal decomposition of carbon into gaseous CO and CO_2 (major and minor products, respectively, cf. Fig. 4c and d) at temperatures above 450 °C.

TPSR experiments of NH_3 production with H_2 and N_2 were performed using the 10Ru/MCP-x samples at 0.1 MPaG and 200–800 °C (Fig. S9). The H_2/N_2 molar ratio was maintained at 3 using a total flow rate of 30 mL min^{-1}, which corresponded to a GHSV of 3500 h^{-1}. Prior to the measurements, the samples were reduced at 350 °C for 2 h under H_2 flow (50 mL min^{-1}). Ammonia formation was observed for 10Ru/ MCP-600–1100 at ~500 °C and found to be minimally influenced by the carbonization temperature. However, monitoring the ammonia formation by 10Ru/MCP-600 with an MS detector was difficult, because it was accompanied by the formation of large amounts of CO and CH_4. In contrast, CO production and CH_4 formation—attributed to the decomposition and methanation of the carbon framework, respectively—were observed at temperatures above 500 °C, which was disproportional to the carbonization temperature of MCP-x, that is, the degree of graphitization. Among the samples, 10Ru/MCP-1100 was conducive to enabling ammonia synthesis at a relatively low temperature (~560 °C at the maximum value), while the reverse was true for CH_4 formation. This suggested that MCP-1100, which was carbonized at a relatively high temperature, was a more suitable support than the other two samples carbonized at lower temperatures. However, the fact that 10Ru/MCP-1100 exhibited the highest ammonia formation at a temperature (~560 °C) that is not very much lower than that for the maximum CH_4 formation (~650 °C) suggested that the catalyst would deactivate during catalytic ammonia synthesis.

3.2.2. Effect of Ru loading (yRu/MCP-1100)

Next, a series of yRu/MCP-1100 samples with MCP-1100 as the support and varied Ru loading (y = 1, 5, or 10 wt%) was prepared by following the same preparation steps for 10Ru/MCP-x; this investigation was aimed at modulating the Ru NP size to study the size-dependent behavior for catalyzing ammonia synthesis. ICP-MS confirmed that the metal loadings of the three samples were close to the nominal values. Notably, the ordered mesostructure of the MCP in the as-prepared yRu/ MCP-1100 samples was retained, as indicated by the small-angle PXRD patterns and nitrogen physisorption isotherms (Figs. S10a and S10c **and** Table S4). The Ru species in the as-prepared samples were so small that no reflections corresponding to any Ru species (metallic Ru or RuO_2) were observed in the wide-angle PXRD patterns (Fig. S10b). TEM images (Fig. S11) indicated that the Ru NP size was positively correlated to the Ru loading, increasing from 1.2 nm for 1Ru/MCP-1100 to 1.4 nm for 5Ru/MCP-1100 and 2.5 nm for 10Ru/MCP-1100. *In situ* XAS measurements at the Ru *K*-edge were performed to study the three samples after reductive activation (by heating under hydrogen flow at 350 °C for 2 h), and the collected spectra were compared with those of Ru foil. XANES data and differential spectra (Figs. S12a **and** b) suggested that the absorption edges of the three samples (corresponding to the 1 s→4p transition) all appeared at 22,117 eV and were identical to that of Ru foil, indicating that the metal species in the three samples were fully reduced in the reductive activation step. k^3-weighted EXAFS spectra were Fourier transformed (FT), and the resulting FT profiles were fit to obtain structural information of the metal (for example, the interatomic distance (R) and coordination number (CN)). All three samples exhibited a relatively weak first-shell peak that corresponded to the Ru–Ru coordination of metallic Ru ($R_{Ru–Ru}$ = 2.63 Å for 1Ru/MCP-1100 and 2.66 Å for 5Ru/MCP-1100 and 10Ru/MCP-1100; cf. $R_{Ru–Ru}$ = 2.67 Å for Ru foil; Fig. S12c **and** Table S5). The intensity of the first-shell peak increased with increasing Ru loading, suggesting the existence of larger Ru NPs at higher metal loadings. Moreover, the CNs determined by fitting for 1Ru/ MCP-1100, 5Ru/MCP-1100, and 10Ru/MCP-1100 were 6.0, 8.5, and 9.1, respectively. The estimated Ru NP sizes for 1Ru/MCP-1100, 5Ru/ MCP-1100, and 10Ru/MCP-1100, calculated using the Ru–Ru CN based on the hexagonal-close-packed Ru structure and by assuming hemispherical geometry, were 0.9, 1.9, and 2.3 nm, respectively. These values are slightly smaller than those obtained by CO chemisorption analysis, probably owing to the Ru NP–C support interactions as well as the Ru NP morphology.

Ammonia synthesis with the yRu/MCP-1100 catalysts (y = 1, 5, or 10 wt%) was surveyed using TPSR measurements (Fig. S13). 1Ru/MCP-1100 did not exhibit any ammonia synthesis activity, but generated methane at temperatures above 550 °C owing to the methanation of the carbon framework. The ammonia synthesis rate increased when the Ru loading was increased from 5 to 10 wt%, and the reaction temperature corresponding to the maximum rate decreased. However, substantial CH_4 formation was observed at higher Ru loadings, presumably owing to the reaction of the carbon framework with more hydrogen spilled over from the Ru surfaces.

3.3. Characterization and catalytic studies of Cs-Ru/MCP-1100 catalysts

3.3.1. Effect of Cs/Ru molar ratio on zCs-10Ru/MCP-1100

To improve the ammonia synthesis activity, Cs_2CO_3 was selected as a Cs precursor and impregnated into 10Ru/MCP-1100, and the Cs/Ru molar ratio (z) was varied in the range 0.5–3. The resulting zCs-10Ru/ MCP-1100 samples were characterized by small- and wide-angle PXRD (Figs. S14a and S14b), and N_2 physisorption analysis (Fig. S14c). In contrast to the small-angle diffraction signals of 10Ru/MCP-1100, those of the 0.5–3Cs-10Ru/MCP-1100 samples at 2θ ≈ 0.95°, 1.60°, and 1.88° were significantly weakened upon increasing the Cs/Ru molar ratio. Similar trends were observed for the graphitic structure in the wide-angle XRD patterns. This implied that either the diffraction contrast decreased when Cs_2CO_3 was present in the composites, or both the mesoporous structure and graphitic framework were progressively affected by the increased impregnation of Cs_2CO_3. N_2 physisorption isotherms (Fig. S14c) indicated that the adsorbed volume decreased and the hysteresis loop at P/P_0 ≈ 0.4–0.6 was truncated with increasing Cs/ Ru molar ratio. The surface area and pore volume of the 0.5–3Cs-10Ru/ MCP-1100 catalysts were slightly lower than those of the 10Ru/MCP-1100 analog (Table S6), potentially indicating that Cs_2CO_3 was loaded onto the basalt-like microstructure and thus influenced the degree of graphitization. The catalyst 2.5Cs-10Ru/MCP-1100 was further analyzed by FE-SEM/EDS and STEM/EDS. The FE-SEM and associated EDS mapping images (Fig. S15) indicated that the mesoporous carbon framework contained numerous nanoparticles, presumably Ru and Cs_2CO_3 species, while the TEM and associated EDS mapping images (Fig. S16) revealed the graphitic nature of MCP-1100 and the hexagonal-close-packed structure of Ru NPs. The CO chemisorption data (Table S6) suggested that the Ru particles in 0.5–3Cs-10Ru/MCP-1100 (2.8–3.7 nm in size) were slightly larger than those in 10Ru/MCP-1100.

Reductive activation of the 0.5–3Cs-10Ru/MCP-1100 samples was studied using the H_2-TPR-MS method (Fig. 5). The resulting profiles could be divided into four ranges: (i) desorption of physically adsorbed water at temperatures below 100 °C, (ii) reduction of RuO_2 to metallic Ru at 100–170 °C, (iii) hydrogenolysis of Cs_2CO_3 to form CsOH with CO_2 release (major reaction) [54,55] and methanation of the carbon framework (minor reaction), and (iv) thermal decomposition of Cs_2CO_3. In Range (i), the water desorption signal (cf. Fig. 5b) was negatively correlated with the Cs/Ru molar ratio, suggesting a decrease in the exposed surface area of the composite materials. In Range (ii), the signal
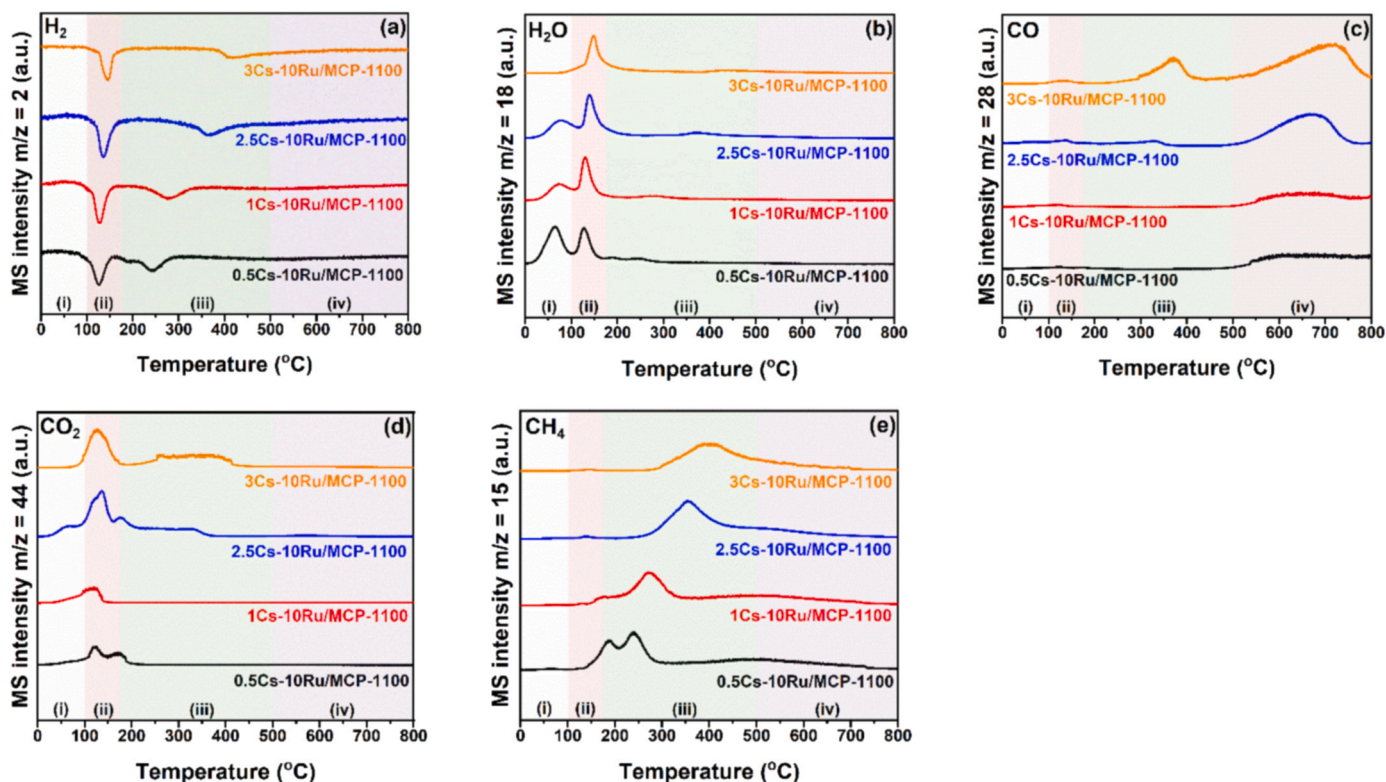
Fig. 5. H$_2$-TPR-MS profiles of Cs-promoted 10Ru/MCP-1100 catalysts with Cs/Ru molar ratios of 0.5–3.

representing the reduction of RuO$_2$ to metallic Ru, accompanied by water formation and CO$_2$ release, shifted to higher temperatures as more Cs was added. This implied the existence of robust Ru–Cs interactions, which hindered the reduction of RuO$_2$. In this step, a small amount of CO$_2$ could react with the hydrogen spilled over from the Ru surface to form CH$_4$. These phenomena are similar to those observed in our recent study on the reduction of Cs-promoted Ru/γ-Al$_2$O$_3$ catalysts [54]. In Range (iii), the hydrogenolysis of Cs$_2$CO$_3$ to form CsOH was also hindered as the Cs content increased. Similar results were observed for methanation of the carbon framework, implying that the Cs$_2$CO$_3$ domain was broadened when more Cs was present in the samples. Similarly, in Range (iv), the signal representing Cs$_2$CO$_3$ decomposition shifted to higher temperatures with increasing Cs/Ru molar ratio.

TPSR profiles of H$_2$ and N$_2$ over various zCs-10Ru/MCP-1100 samples were obtained to evaluate the ammonia synthesis activity and carbon framework methanation (Fig. 6 and S17). The analysis procedure was the same as that employed for obtaining the results shown in Fig. S9 and Fig. S13. All samples exhibited increased ammonia synthesis rates as the reaction temperature was increased to 300 °C or higher, and the maximum ammonia synthesis rate varied with the Cs/Ru molar ratio. Among them, 2.5-Cs-10Ru/MCP-1100 and 3Cs-10Ru/MCP-1100 exhibited the highest ammonia synthesis rate of 7.8–7.9 mmol$_{NH3}$ g^{-1} h^{-1} at 370–380 °C and 0.1 MPa. The ammonia synthesis rate of 3Cs-10Ru/MCP-1100 closely resembled that of 2.5Cs-10Ru/MCP-1100, indicating that the adding more Cs species had no significant impact on the improvement of ammonia synthesis at the active sites. When the Cs/Ru molar ratio was decreased to 1 and further to 0.5, the maximum ammonia synthesis rate decreased and the corresponding temperature shifted toward higher temperatures ($> \sim$400 °C). All catalysts generated methane at temperatures above 400 °C owing to the methanation of the
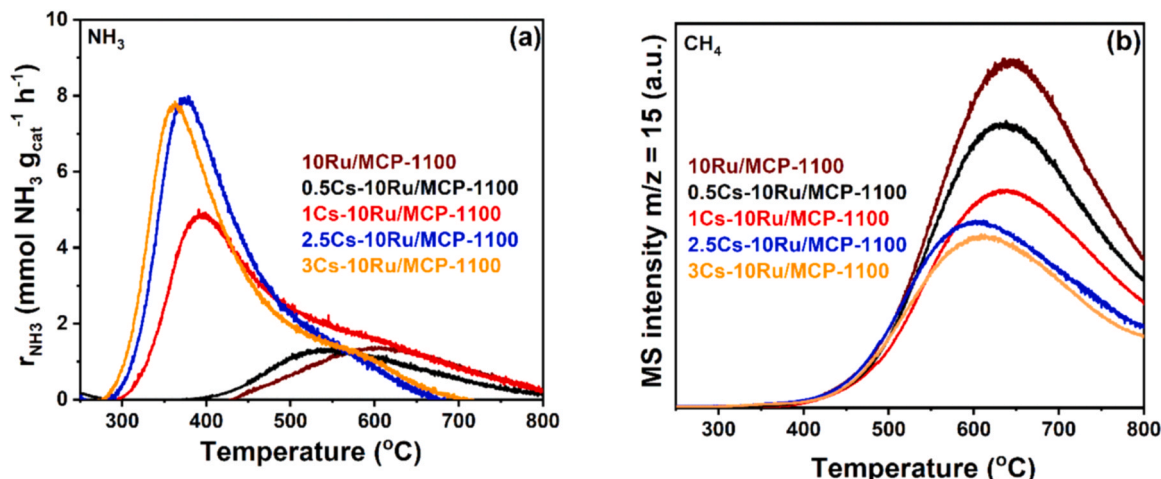

Fig. 6. TPSR profiles for ammonia synthesis over 0.5–3Cs-10Ru/MCP-1100 catalysts.

carbon framework with hydrogen spilled over on the Ru surface. Interestingly, the methanation signal intensity decreased as the Cs/Ru molar ratio increased, leading to speculation that the presence of Cs species may play a crucial role in suppressing the reaction between the spillover hydrogen and carbon framework, while effectively enhancing the activity of Ru NPs in ammonia synthesis.

3.3.2. Effect of carbonization temperature on 2.5Cs-10Ru/MCP-x

To correlate the carbonization temperature and ammonia synthesis activity, 2.5Cs-10Ru/MCP-x samples containing MCP-x produced at various carbonization temperatures were prepared and characterized by small- and wide-angle PXRD and N_2 physisorption analysis (Fig. S18). The small-angle diffraction signals of all 2.5Cs-10Ru/MCP-x samples disappeared after a large amount of Cs_2CO_3 (29 wt%) was impregnated. This result is similar to that of the 0.5–3Cs-10Ru/MCP-1100 samples, presumably because of the impregnation of a large amount of Cs_2CO_3 (~7–29 wt%). Although the adsorbed nitrogen volume decreased, the shapes of the N_2 physisorption isotherms of 2.5Cs-10Ru/MCP-x (Fig. S18c) were similar to those of MCP-x (Fig. 1b) and 10Ru/MCP-x (Fig. 3c), indicating that the Cs impregnation minimally influenced the nanostructure of the mesoporous carbon framework. Furthermore, the surface area and pore volume decreased with increasing carbonization temperature (Table S7). Moreover, the CO chemisorption results indicated that the Ru NP sizes ranged from 3 to 4 nm and were slightly influenced by the carbonization temperature.

Reductive activation and the performance of the 2.5Cs-10Ru/MCP-x samples prepared at carbonization temperatures of 600, 850, and 1100 °C were studied by H_2-TPR-MS and TPSR-MS, respectively. Similar H_2-TPR-MS profiles were obtained for the three samples (Fig. S19), with four zones being observed: desorption of physically adsorbed water, reduction of RuO_2 to metallic Ru, hydrogenolysis of Cs_2CO_3 to CsOH, and thermal decomposition of Cs_2CO_3 (major) and the carbon framework (minor) at 30–100, 100–170, 200–500, and 500–700 °C, respectively. Notably, methane production was observed over a wide temperature range (500–700 °C), and its relative magnitude was not in proportion to the carbonization temperature. 2.5Cs-10Ru/MCP-600 displayed a considerably stronger methane signal than that of the other two samples. MCP-600, which was prepared at a low carbonization temperature, contained numerous oxygenated groups that evidently reacted with the hydrogen spilling over from the Ru surface to produce methane.

The ambient-pressure ammonia synthesis activity of the 2.5Cs-10Ru/MCP-x samples was screened by TPSR analysis (Fig. 7). Both 2.5Cs-10Ru/MCP-850 and 2.5Cs-10Ru/MCP-1100 exhibited high ammonia synthesis rates (7.3–7.9 $mmol_{NH3}$ g^{-1} h^{-1}) at 380–400 °C and 0.1 MPa and formed methane at temperatures above 400 °C, the amount of

which decreased slightly with increasing carbonization temperature (800–1100 °C). Analysis of the relative methane generation area shown in Fig. 7b indicated that 2.5Cs-10Ru/MCP-650 and 2.5Cs-10Ru/MCP-800 produced 26% and 3% more methane than that generated by 2.5Cs-10Ru/MCP-1100. 2.5Cs-10Ru/MCP-600 exhibited a relatively low ammonia synthesis rate (5.4 $mmol_{NH3}$ g^{-1} h^{-1}) at a relatively high temperature of 425 °C and produced a significant amount of methane at this temperature. Consequently, 2.5Cs-10Ru/MCP-600 was deemed unsuitable for ammonia synthesis at mild temperatures (~400 °C) owing to the methanation-induced loss of the carbon framework. Therefore, 2.5Cs-10Ru/MCP-800 and, in particular, 2.5Cs-10Ru/MCP-1100 were considered to suitably catalyze ammonia synthesis.

3.3.3. Effect of Ru particle size on 2.5Cs-yRu/MCP-1100

2.5Cs-yRu/MCP-1100 samples with various Ru loadings were prepared and characterized in the same manner as described above. It is worth noting that, at a fixed Cs/Ru molar ratio of 2.5, the amount of Cs_2CO_3 impregnated also increased with increasing Ru loading. Small-angle diffraction signals of 2.5Cs-1Ru/MCP-1100 and 2.5Cs-5Ru/MCP-1100 with nominal Cs loadings of 4–29 wt% and a nominal Ru loading of 1–5 wt% were observed (Fig. S20a). In contrast, that of 2.5Cs-10Ru/MCP-1100 was not observed owing to the large amounts of impregnated Ru (10 wt%) and Cs (33 wt%). In the wide-angle XRD patterns, peaks representing Cs and Ru species were not observed, indicating adequate dispersion of these species in the 2.5Cs-yRu/MCP-1100 samples (Fig. S20b). However, graphitic-structure-related peaks appeared at $2\theta = 0.9°$, $1.6°$, and $1.9°$ for 2.5Cs-1Ru/MCP-1100, whereas they were absent in the patterns of the other two samples with higher Ru and Cs loadings (Ru = 5–10 wt% and a fixed Cs/Ru molar ratio of 2.5). This was probably associated with the reduced difference in electron density between the carbon framework and the large amount of impregnated Cs species. The hysteresis loops in the N_2 physisorption isotherms gradually contracted as the loadings of Ru and Cs_2CO_3 simultaneously increased (Fig. S20c). CO chemisorption analysis (Table S8) suggested that the extent of CO uptake was positively correlated with the weight percentage of Ru, whereas the particle size showed a negative correlation owing to the higher dispersion obtained when small amounts of Ru were added.

The TPSR profile of 2.5Cs-1Ru/MCP-1100 (Fig. S21) highlighted the lack of activity. Notably, 2.5Cs-10Ru/MCP-1100 maintained the highest ammonia synthesis rate among the catalysts, which was consistent with the TPSR profiles of the yRu/MCP-1100 samples. A comparison of the relative methane generation area, as depicted in Fig. S21b, indicated that 2.5Cs-1Ru/MCP-1100 and 2.5Cs-5Ru/MCP-1100 produced 38% and more 11% methane, respectively, than that generated by 2.5Cs-10Ru/MCP-1100. However, this result differed from that observed in
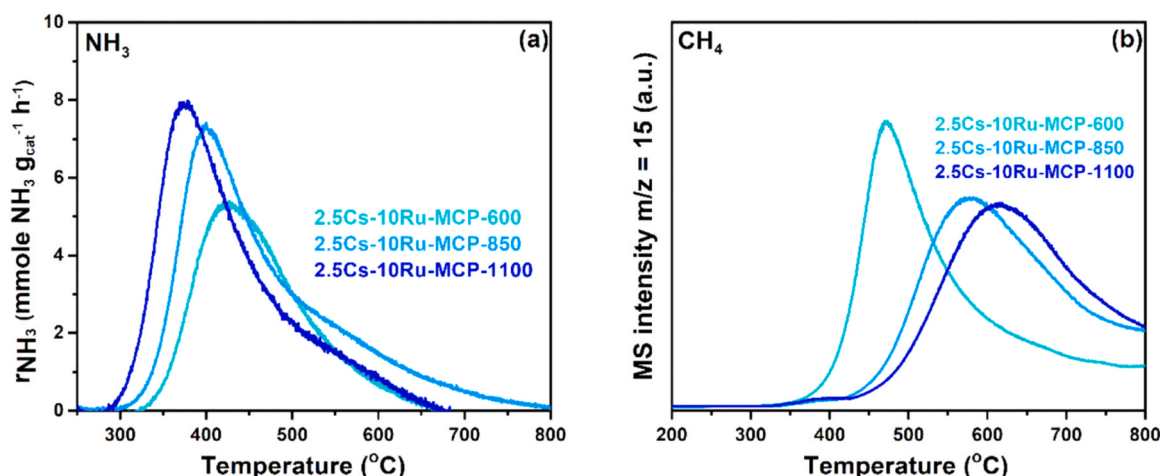

Fig. 7. TPSR profiles for ammonia synthesis over the 2.5Cs-10Ru/MCP-x catalysts.

the *y*Ru/MCP-1100 series, presumably due to the impregnation of Cs$_2$CO$_3$. It was speculated that the degree of methanation was not only associated with Ru loading for 2.5Cs-10Ru/MCP-1100 but also related to the Cs/Ru molar ratio, which may influence the proximity of Cs to Ru and, consequently, affect their interaction. The spent (used) 2.5Cs-10Ru/MCP-1100 after TPSR measurement of NH$_3$ synthesis at 400 ºC and 0.1 MPa for 3 h was characterized (Fig. S22). Wide-angle PXRD revealed small degree of sintering of the metallic Ru in the used 2.5Cs-10Ru/MCP-1100, while air-TGA analysis indicated a slight loss (~2 wt %) of carbon of the support, presumably through methanation and thermal decomposition of carbon framework. As compared to the as-prepared catalyst, the used 2.5Cs-10Ru/MCP-1100 exhibited slightly decreased surface area and porosity (determined by N$_2$ physisorption) but showed a slightly higher CO uptake (determined by CO chemisorption, cf. Table S8). The changes in textural properties and CO uptake may be associated to factors including small degree of Ru sintering, slight loss of carbon support, and redistribution/relocation of Cs species. Finally, the Raman spectrum of the used catalyst is similar to that of the as-prepared catalyst, indicating that the structure of MCP-1100 was not significantly altered during TPSR.

3.4. Pressurized ammonia synthesis

Pressurized ammonia synthesis was investigated in a stainless-steel fixed-bed reactor using 0.5–3Cs-10Ru/MCP-1100 catalysts at 0.9 MPaG and 250–500 °C. A mixed H$_2$/N$_2$ gas (H$_2$/N$_2$ molar ratio = 3, 120 mL min^{-1}) was used as a feedstock to achieve a GHSV of 6600 h^{-1}. The ammonia synthesis rate and yield of the 0.5–3Cs-10Ru/MCP-1100 catalysts were monitored with respect to the reaction temperature (Fig. 8). Kinetic analysis and DFT calculations were performed (as discussed later in Section 3.6) to compare the structural properties of the composite catalysts. Among the investigated catalysts, 2.5Cs-10Ru/MCP-1100 and 3Cs-10Ru/MCP-1100 exhibited the highest ammonia synthesis rate and yield (~44 mmol g^{-1} h^{-1} and ~2.8 vol%, respectively) at the lowest reaction temperature of 400 °C. The ammonia synthesis rate and yield decreased for lower Cs/Ru molar ratios (0.5–1); moreover, the corresponding temperatures were higher. Ru/MCP-1100 exhibited extremely low activity under the studied conditions, indicating that the addition of Cs significantly promoted the activity of the Ru catalyst for ammonia synthesis. Ammonia synthesis performed using the 2.5Cs-10Ru/MCP-1100 catalyst at 0.9 MPaG was compared with that under ambient pressure (Fig. 9), with other parameters such as the

H$_2$/N$_2$ molar ratio, flow rate, and catalyst weight being similar. At 0.1 MPa, the ammonia yield and synthesis rate at 280–300 °C were ~0.1 NH$_3$% and 1.5 mmol$_{NH3}$ g^{-1} h^{-1}, respectively, and the maximum ammonia yield (0.9. vol%) and synthesis rate (14.6 mmol$_{NH3}$ g^{-1} h^{-1}) were achieved at 370 °C. With a further increase in the reaction temperature, the ammonia yield and synthesis rate decreased owing to thermodynamic equilibrium, because the reverse reaction (that is, ammonia decomposition) was faster than the forward reaction (that is, ammonia formation). However, when the reaction pressure was increased to 0.9 MPaG, the ammonia rate and yield increased to 42.8 mmol$_{NH3}$ g^{-1} h^{-1} and 2.7 vol%, respectively; moreover, the corresponding reaction temperature also increased to 410 °C because of hydrogen poisoning.

3.5. Intermittent ammonia synthesis

Ammonia synthesis over 2.5Cs-10Ru/MCP-1100 under intermittent operating conditions was further investigated in the temperature range of 250–410 °C at a constant pressure (0.9 MPaG) and H$_2$/N$_2$ molar ratio (3; GHSV = 6000 h^{-1}) for three cycles lasting ~92 h (Fig. 10 and S23). The reaction temperature was maintained at 250 °C after each cycle while the reaction gas was switched to N$_2$, and the reaction pressure was reduced from 0.9 MPa to 0.1 MPa for 4 h prior to the next cycle. This measurement cycle simulates electrolytic H$_2$ production using renewable electricity, which varies with the weather and local environment. In the first cycle, the ammonia synthesis rate over 2.5Cs-10Ru/MCP-1100 increased with increasing reaction temperature from 250 to 410 °C, whereas the reverse trend was observed when the reaction temperature was decreased from 410 to 250 °C. A slight hysteresis loop was observed during the heating–cooling cycle for the reaction-temperature-dependent ammonia synthesis rate and yield (Fig. S24). Similar phenomena were observed in the second and third cycles. However, the hysteresis loop became narrower, because the curve corresponding to the increasing reaction temperature gradually approached that for the decreasing reaction temperature. This suggests that the active sites of 2.5Cs-10Ru/MCP-100 were readily stabilized during intermittent ammonia synthesis. This behavior differs from that of Fe-based catalysts, in which the active sites are significantly affected by intermittent conditions, such as the reaction temperature and the composition and pressure of flowing gas, resulting in a broad hysteresis phenomenon in ammonia synthesis, as recently discussed by Aika *et al.* at the TOCAT9 conference [56]. The discussion highlighted the significant impact of
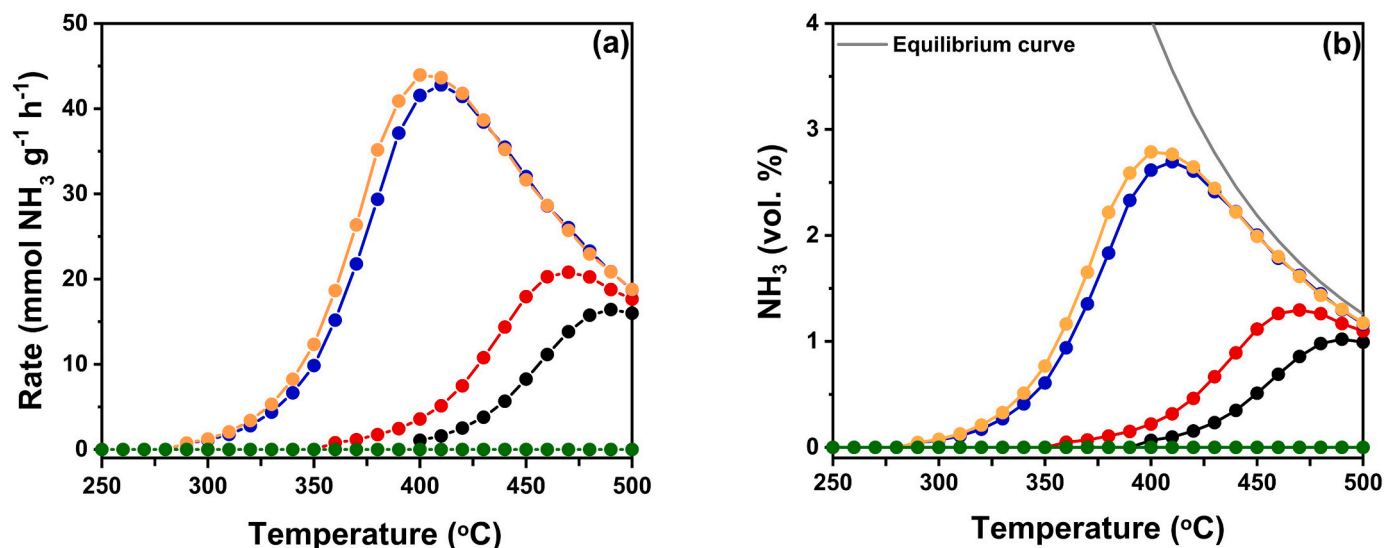

Fig. 8. Temperature dependence of the (a) ammonia synthesis rate and (b) ammonia yield over (●) 10Ru/MCP-1100, (●) 0.5Cs-10Ru/MCP-1100, (●) 1Cs-10Ru/MCP1100, (●) 2.5Cs-10Ru/MCP-1100, and (●) 3Cs-10Ru/MCP-1100 at 0.9 MPaG.
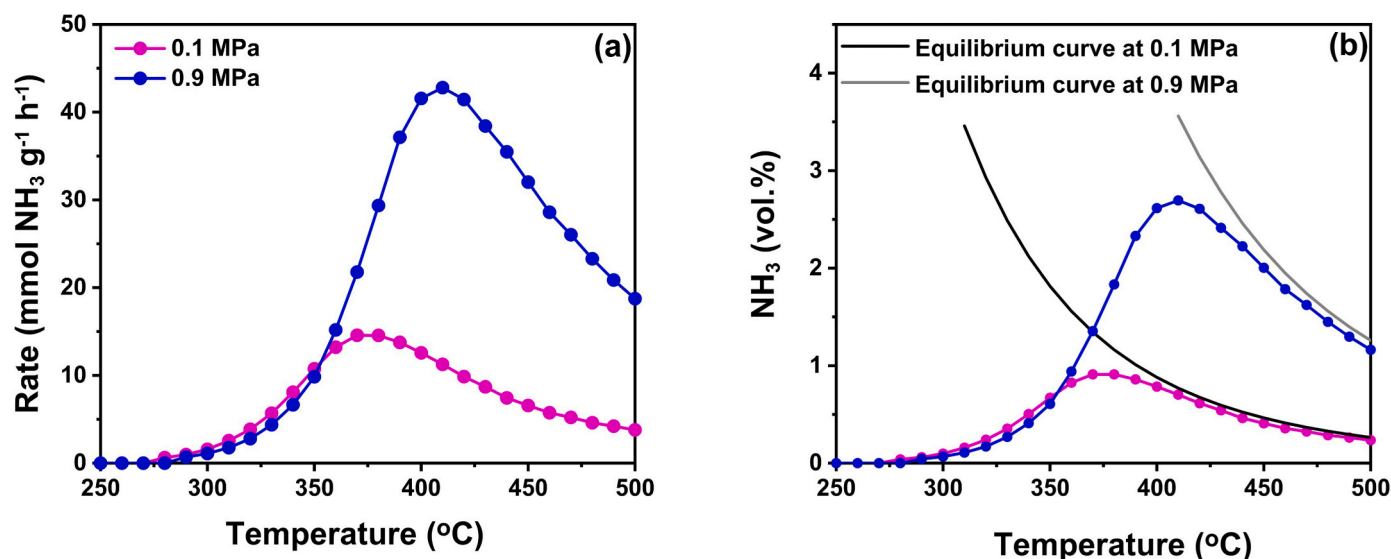
Fig. 9. . Temperature dependence of (a) ammonia synthesis rate and (b) ammonia yield over the 2.5Cs-10Ru/MCP-1100 catalyst at (●) 0.1 and (●) 0.9 MPaG.
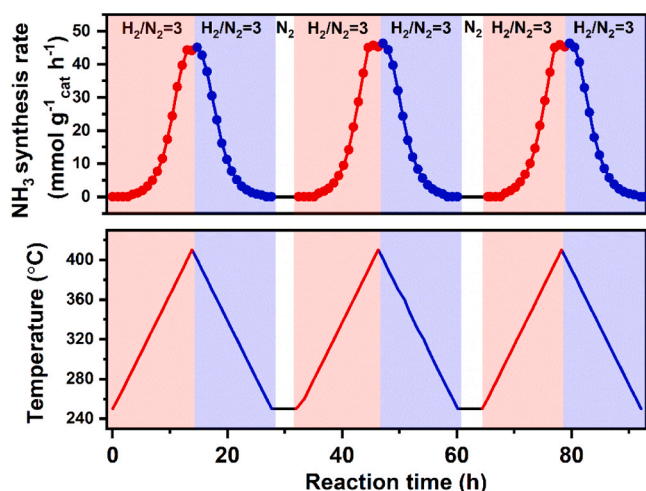

Fig. 10. Temperature dependence of ammonia synthesis rate over 2.5Cs-10Ru/MCP-1100 under intermittent operating conditions.

switching reactant gases on the active components enabling green ammonia synthesis via the eHB process.

3.6. Mechanistic studies

3.6.1. In situ XAS and NAP-XPS

The ammonia synthesis activity of the 2.5Cs-10Ru/MCP-1100 catalyst is similar to those various previously reported carbon-supported Ru catalysts with single- or multi-element promoters (Table 1). However, the effect of the degree of graphitization of carbon on the formation of active components, including active sites and promoters, has not been comprehensively discussed. Based on the results of in-situ XRD and H_2-TPR-MS, Raróg-Pilecka *et al.* suggested the formation of partially reduced Cs_xO_y species ($x/y = 2.7–3.6$) from cesium nitrate ($CsNO_3$) during reductive activation of the activated carbon-supported Ru catalysts [57]. Recent studies have demonstrated that the active components of Cs-promoted Ru catalysts formed by reductive activation are influenced by the conditions employed for ammonia synthesis [21,23,54,55]. Therefore, in this study, the oxidation states of the Cs-promoted Ru catalysts were studied by in situ XAS and NAP-XPS and were correlated with the function of the active components in enabling ammonia

synthesis. Samples with 10 wt% Ru and a Cs/Ru molar ratio of 2.5 (that is, 2.5Cs-10Ru/MCP-*x*) were selected, and the spectra of the samples before and after reduction activation were compared (the reduced samples are designated as 2.5Cs-10Ru/MCP-*x*-R). In the obtained Cs L_3-edge XANES spectra (Fig. 11a–c), all samples showed a relatively sharp absorption edge at ~5015 eV prior to reductive activation. Notably, the edge position remained nearly unchanged while the white-line intensity decreased after the reductive activation at 350 °C under hydrogen flow. This phenomenon is associated with an increase in the d-state electron density involved in the 2p–3d resonance transition [58,59], thereby indicating the partial reduction of Cs^{1+} in the three samples to Cs^0. The difference in the white-line intensity before and after reductive activation (ΔI_{WL}) was considerably larger for 2.5Cs-10Ru/MCP-1100 (ΔI_{WL} = 0.23) than that for 2.5Cs-10Ru/MCP-850 (ΔI_{WL} = 0.13) and 2.5Cs-10Ru/MCP-600 (ΔI_{WL} = 0.15). Moreover, the value for 2.5Cs-10Ru/MCP-1100 is significantly larger than that of our previously studied γ-Al_2O_3-supported Cs-promoted Ru catalysts [54]. This comparison implies that a higher degree of graphitization for the carbon support may facilitate the production of more Cs^0 as a dynamic species during reductive activation and even under catalytic reaction conditions. It is noted that, based on in-situ XAS study, Rossetti *et al.* also suggested that the chemical environment of Cs could be influenced by the presence of Ru and the graphitization degree of carbon support [58].

To perform the in situ NAP-XPS measurements, the 2.5Cs-10Ru/MCP-*x* samples were first evacuated at 25 °C and then analyzed. Subsequently, the samples were reduced with H_2 (2 mbar) at 350 °C for 20 min before being cooled to 25 °C and measured again with background H_2 at a pressure of 0.2 mbar. Considering the in situ NAP-XPS profiles of the Cs 3d region (Fig. 11d–f), all three samples exhibited similar spectra and nearly identical changes, that is, the peaks corresponding to Cs $3d_{5/2}$ and $3d_{3/2}$ shifted toward higher energies after reduction activation, with the Cs $3d_{5/2}$ binding energy increasing from 724.7 to 725.5 eV. While a shift toward a higher binding energy typically suggests oxidation of the element, the opposite has been observed for Cs and other metals including Ag, Cd, and Ba [60–63]. The value of 724.7 eV is between those found for thin surface layers of cesium oxide (Cs_2O; 725.2 eV) and cesium peroxide (Cs_2O_2; 724.5 eV) on different substrates [60,61], whereas the value of 725.5 eV is lower than that for Cs metal (726.1 eV) [62] and identical to that for cesium suboxide on a silver substrate ($Cs_{2+x}O$; 725.5 eV) [60]. Additionally, the Cs $3d_{5/2}$ peaks in the three sample spectra were slightly wider (~2.5–2.8 eV) than those reported for Cs-modified graphitic-carbon-supported Ru
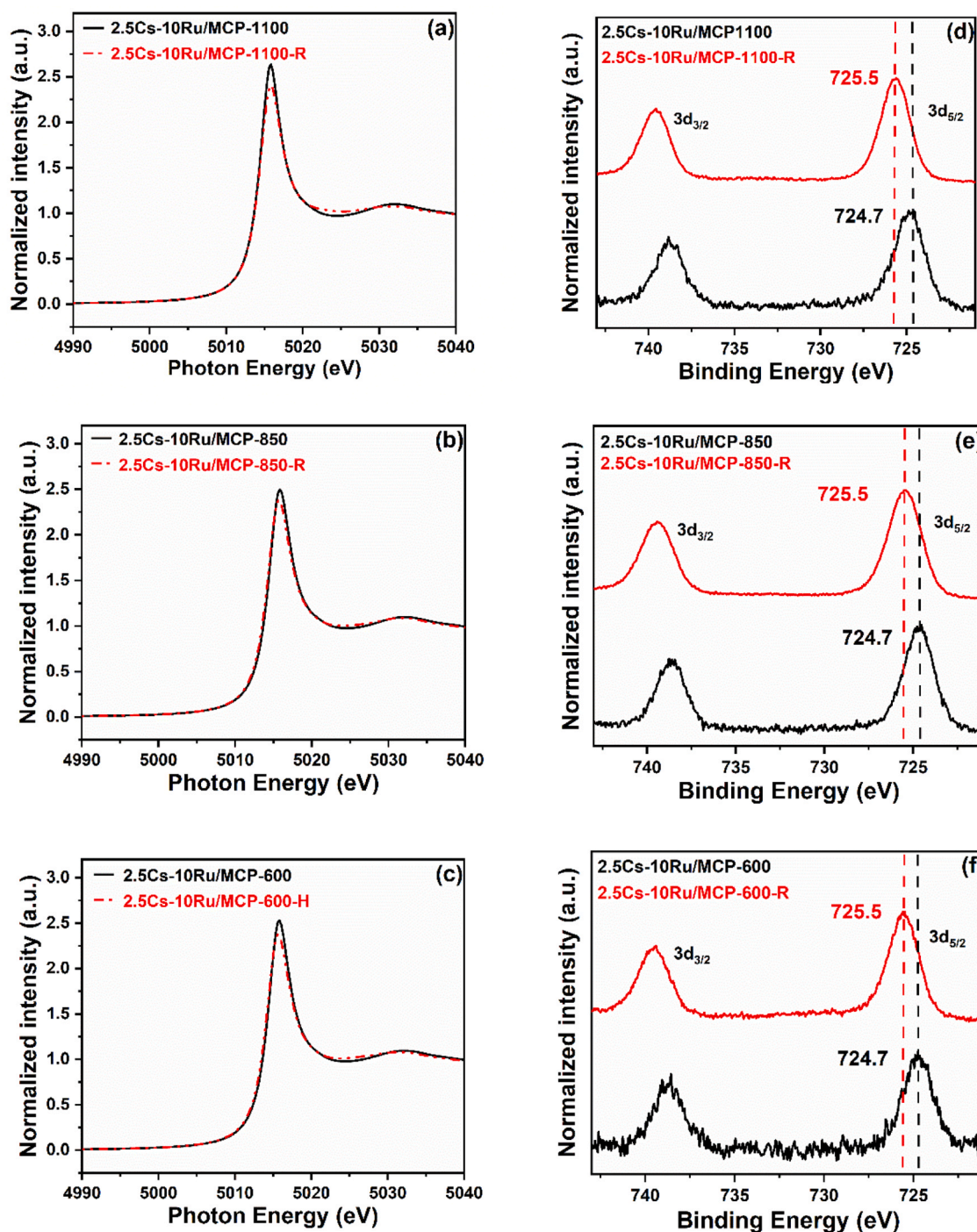
Fig. 11. Results of in situ XAS and NAP-XPS measurements. (a–c) XANES spectra at the Cs L_3-edge, and (d-f) NAP-XPS profiles of the Cs3d region.

catalysts (~2.0–2.2 eV) [62]. Given that some of the supported Cs species were directly attached to Ru, multiple types of Cs species with distinct oxidation states were probably present simultaneously on the surfaces of the composite catalysts. Therefore, the Cs $3d_{5/2}$ peaks in the spectra of the three catalysts were further analyzed and deconvoluted into two peaks with reported values for the most probable Cs species (that is, Cs_2O and Cs_2O_2 for 2.5Cs-10Ru/MCP-x; Cs_2O and Cs metal for 2.5Cs-10Ru/MCP-x-R). The resulting fits (Fig. S25) suggested that the Cs precursor in 2.5Cs-10Ru/MCP-x (Cs_2CO_3) partially decomposed (~38–47%) and transformed to Cs_2O_2 during the evacuation, and that approximately half of the Cs species were reduced to Cs^0 after reduction activation under 2 mbar of H_2. The degree of Cs reduction for

2.5Cs-10Ru/MCP-1100 was significantly higher (60%) than that for 2.5Cs-10Ru/MCP-850 and 2.5Cs-10Ru/MCP-600. Overall, the in situ XAS and NAP-XPS results confirmed that, despite the difference in the measurement conditions, part of the Cs species was reduced to Cs^0 in the reductive atmosphere at 350 °C, and that a higher degree of graphitization of the carbon support was favored.

In the in situ NAP-XPS profiles of the C1s/Ru3d region (Fig. S26), the spectra of 2.5Cs-10Ru/MCP-x mainly showed two peaks, with the one at 281.0–281.3 eV assigned to the Ru $3d_{5/2}$ peak of RuO_2 [64] and the other at 284.5–284.7 eV having contributions from the C 1s peak (284.4–285.0 eV for the carbon atoms surrounded only by carbon atoms (C–C)) [65,66] and the Ru $3d_{3/2}$ peak (~284.8–285.0 eV) of RuO_2 [64].

The tailing of the latter peak toward higher binding energies was probably due to carbon atoms singly bound to an oxygen atom (C–O) with a binding energy of ~286–287 eV [65,66]. A comparison of the values for 2.5Cs-10Ru/MCP-1100 and the Cs-free sample (10Ru/MCP-1100) suggests that the presence of Cs species had a negligible influence on the chemical state of the Ru species and the carbon support in the unactivated samples. After reductive activation, the Ru $3d_{5/2}$ peak shifted to ~280.1 eV, indicating complete reduction of the metal, while the combined C 1 s and Ru $3d_{3/2}$ peaks remained nearly unchanged. Notably, an additional peak appeared at 289.5 eV in the spectra of the catalysts supported on MCP-850 and MCP-1100, but not in the those of 2.5Cs-10Ru/MCP-600-R and 10Ru/MCP-1100-R. Because this peak may be attributed to carbon atoms doubly bonded to oxygen atoms (C=O) [65,66], the appearance of this peak seems to imply that the presence of Cs species might facilitate the partial oxidation of surface carbon atoms in the catalysts with MCP-850 and MCP-1100. Although the exact reasons remain unknown, we speculate that, as a basic species generated from the hydrogenolysis of Cs_2CO_3, the CsOH at the interface of Ru and carbon support might react and oxidize the nearby surface carbons. Besides, it might be also correlated to the surface concentrations of Cs and Ru in the catalysts. Further analyses are in progress to get better understanding of why such a peak at 289.5 eV appeared after reductive activation for the two catalysts.

3.6.2. Kinetic analysis and TPD studies

Table 4 shows the kinetic analysis results of 2.5Cs-10Ru/MCP-1100 employed for ammonia synthesis at 380 °C and 0.9 MPa, in comparison with previously reported catalysts with similar Ru loadings and Cs/Ru molar ratios measured under similar conditions. All the catalysts yielded a reaction order n close to 1, which corresponded to N_2 species, indicating that the rate-determining step of ammonia synthesis over the Cs-promoted Ru catalyst was N_2 dissociation [54]. The reaction order h, corresponding to H_2 species, was approximately -0.9 to -0.3, whereas the order a, corresponding to NH_3 species—was approximately 0 to –0.24. This suggested that all the catalysts experienced H_2 poisoning rather than NH_3 inhibition. As compared to 2.5Cs-10Ru/SGCNT and 2.5Cs-10Ru/MPC, the kinetic behavior of 2.5Cs-10Ru/MCP-1100 was more similar to that of 1.5Cs-5Ru/γ-Al$_2$O$_3$, (for example, the relatively negative value of h (approximately -0.5) and relatively positive value of a (approximately -0.2)) presumably owing to the relatively acidic surface of 2.5Cs-Ru/MCP-1100, which was carbonized at 1100 °C, with oxygenated groups on the carbon framework. These oxygenated groups can be removed by graphitization of the carbon materials at higher temperatures, such as annealing the MPC sample at 1500–2100 °C in inert gas. Nevertheless, the significant CO_2 emissions resulting from the hazardous carbonization conditions remains an ongoing challenge.

The reaction intermediate species adsorbed onto the active components of the Cs-promoted Ru catalysts, which were reductively activated and involved in reacting in the ammonia synthesis, were studied by TPD-MS, particularly for monitoring the H_2, N_2, and NH_x species (Fig. 12). The NH_3 species were nearly invisible, presumably owing to the decomposition of the adsorbed NH_x species into H_2 and N_2 prior to the TPD-MS measurements (Fig. S27a). A small signal appeared at temperatures below 200 °C, evidently due to the release of water (Fig. S27b). The presence of N_2 species (the β_{N2} zone in Fig. 12a), which was monitored using the m/z ratios of N (14; Fig. S27c) and N_2 (28), was categorically related to the Cs/Ru molar ratios of the studied catalysts (Fig. 12a'). For 10Ru/MCP-1100 and 0.5–1Cs-10Ru/MCP-1100, a strong signal (denoted as γ_{CO}) appeared at temperatures above 400 °C; this was associated with CO formation via the thermal decomposition of the MCP-1100 carbon framework, which was identified by m/z values of C (12) and CO (28) (Fig. S27d, e). The phenomenon is similar to what Ni *et al.* observed for the potassium-promoted activated carbon-supported Ru catalysts, which generated CO during the deactivation at temperatures higher than 500 °C due to the decomposition of surface oxygenates of AC [67]. In contrast, this γ_{CO} signal appeared at 450–700 °C for the 2.5–3Cs-10Ru/MCP-1100 catalysts. This phenomenon seemingly involved a more pronounced release of CO through the decomposition of Cs_2CO_3 that was impregnated substantially in the 2.5–3Cs-10Ru/MCP-1100 catalysts, compared to the decomposition of the carbon framework. This result is another indication that the surface of the 2.5–3Cs-10Ru/MCP-1100 catalysts could be fully covered with Cs_2CO_3 species. Additionally, three signals of H_2 species—monitored using an m/z ratio of 2—were observed at temperatures below 200 °C, in the 250–450 °C range, and above 400 °C (termed α_{H2}, β_{H2}, and γ_{H2}, respectively) (Fig. 12b). The α_{H2} signal might be associated with surface NH_x species, which decomposed into H_2 and N_2 species that were partly adsorbed onto the catalyst surface and then desorbed at temperatures below 200 °C. The γ_{H2} signal was possibly related to the strongly adsorbed H_2 species on the Ru surface, presumably owing to the hydrogen poisoning. Notably, an additional β_{H2} signal was exhibited by the 2.5~ 3Cs-10Ru/MCP-1100 catalysts, while the α_{H2} and γ_{H2} signals shifted slightly toward high temperatures. This indicated that the presence of a certain amount of Cs could help tune the surface properties of the prepared catalysts, by making them more basic, for instance, which could reduce hydrogen poisoning due to spillover effect.

3.6.3. Mechanistic understanding of hydrogen spillover by DFT calculations

To elucidate the effects of the promoter on the hydrogen spillover mechanism, three simple models were constructed using single-vacancy graphene (SVG) as the support for adsorbing a (i) Ru atom (Ru/SVG, Fig. 13a), (ii) Ru atom bound to a Cs atom (Ru–Cs/SVG, Fig. 13b), and (iii) Ru atom bound to CsOH species (Ru–CsOH/SVG, Fig. 13c). Notably, these three models exclude the effects of the morphology and interactions between the Ru particles and carbon support. The three models were intentionally subjected to saturated hydrogen adsorption, and the results showed that six hydrogen molecules were adsorbed onto the modeled structures (Fig. S28). To simulate the hydrogen spillover, a H atom was deliberately moved from Ru to SVG in the three models through transition states to form thermodynamically stable states. The E_a values for hydrogen spillover in the Ru/SVG and Ru–Cs/SVG models (2.25–2.27 eV; Fig. 13a,b) indicated that Cs^0 barely influenced the hydrogen spillover mechanism. However, the lower E_a value for hydrogen spillover in Ru–CsOH/SVG (0.87 eV; Fig. 13c) demonstrated that CsOH facilitated the hydrogen spillover mechanism and possibly mitigated the hydrogen poisoning in ammonia synthesis. This DFT calculation is in agreement with experimental data, revealing that hydrogen adsorbed on the Ru surface may spill over to CsOH species or nearby locations, thereby reducing the hydrogen poisoning effect.

4. Conclusions

The impact of the graphitization degree of the carbon support for Ru catalysts on ammonia synthesis was systematically studied using a series

Table 4
Kinetic analysis and turnover frequency of Cs-Ru catalysts.

Catalyst	h	n	a	TOF (s^{-1})	Reference
2.5Cs-10Ru/ MCP-1100[a]	-0.50	0.88	-0.24	0.046	Present study
2.5Cs-10Ru/ SGCNT[b]	-0.51	0.99	-0.02	0.038	[23]
2.5Cs-10Ru/ MPC[c]	-0.90	0.95	-0.03	0.062	[23]
1.5Cs-Ru/ γ-Al$_2$O$_3$[d]	-0.30	0.90	-0.20	0.049	[54]

[a] Reaction order and TOF determined at 0.9 MPa and 380 °C, and 0.9 MPa and 410 °C, respectively.

[b] Reaction order and TOF determined at 0.9 MPa and 380 °C, and 0.9 MPa and 400 °C, respectively.

[c] Reaction order and TOF determined at 0.9 MPa and 380 °C, and 1 MPa and 400 °C, respectively.

[d] Reaction order and TOF determined at 1 MPa and 430 °C, and 1 MPa and 410 °C, respectively.
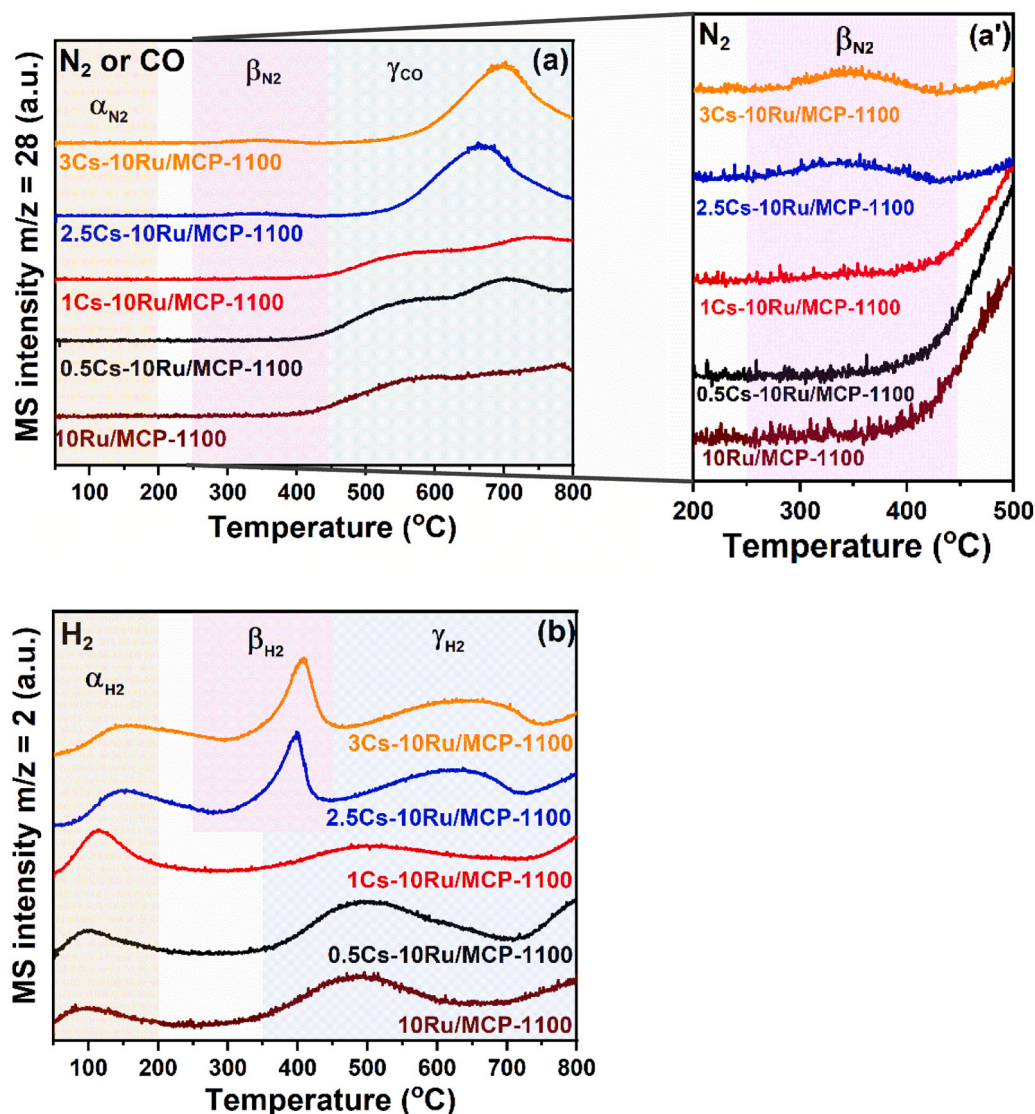
Fig. 12. TPD-MS profiles of (a) N_2 and CO signals (monitored and identified using m/z ratios of 12, 14, and 28) and (b) H_2 signal (monitored using an m/z ratio of 2) over the 0- to 3Cs-10Ru/MCP-1100 catalysts after NH_3 synthesis at 400 °C and 0.1 MPa for 1 h; the N_2 signal in the 200–500 °C range in (a) is enlarged in (a').

of ordered MCPs with similar textural properties but different degrees of graphitization as supports to prepare Cs-promoted Ru catalysts. The influences of the graphitization degree of the support, Ru particle size, and Cs/Ru molar ratio on the catalytic behavior for ammonia synthesis were clearly revealed. Reductive activation of the catalysts was studied using multiple techniques including H_2-TGA, TPR-MS, in situ XAS, and in situ NAP-XPS, and combined with the results of DFT calculations. The results showed that a higher degree of graphitization was beneficial for stabilizing the carbon support against methanation during ammonia synthesis. Additionally, both Cs^0 and CsOH were formed as dynamic species under reductive activation, with a significant quantity of Cs^0 being produced in the catalysts supported on MCPs with a higher degree of graphitization. The prepared catalyst that gave high performance was supported on MCP-1100 with the highest graphitization degree among the other catalysts. It featured a Ru NP size of 2.3 nm (corresponding to 10 wt% Ru) and a Cs/Ru molar ratio of 2.5. The catalyst exhibited ammonia synthesis rates of 7.9 at 370 °C and 0.1 MPa, as well as 43 $mmol_{NH3}$ g^{-1} h^{-1} at 410 °C and 0.9 MPa. Ammonia synthesis was effectively conducted using this catalyst under intermittent operating conditions. The presence of CsOH species played a critical role in facilitating hydrogen spillover from the Ru surface, thereby mitigating

hydrogen poisoning on the Ru surfaces. This process resulted in the generation of Cs^0 species, which donated electrons to the Ru surfaces, enhancing N_2 adsorption/activation, and, consequently boosting ammonia synthesis at milder conditions while preventing carbon support methanation. Our findings provide valuable insight into how the graphitization degree enhances the stability of carbon-based catalysts, and the formation of effective Cs species that boost Ru catalysts for milder ammonia synthesis. These insights can be readily applied to the development of new metal catalysts promoted with alkali and alkaline earth metal and supported on the carbon materials, thereby expanding their potential applications for industrial catalytic processes.

CRediT authorship contribution statement

Keller Martin: Formal analysis, Writing – review & editing. **Nishi Masayasu:** Investigation, Project administration, Supervision, Writing – review & editing. **Mochizuki Takehisa:** Project administration, Supervision, Writing – review & editing. **Chang Chih-Li:** Writing – review & editing. **Chou Ho-Hsiu:** Funding acquisition, Project administration, Supervision, Writing – review & editing. **Chen Hsin-Yi Tiffany:** Funding acquisition, Methodology, Project administration, Supervision, Writing
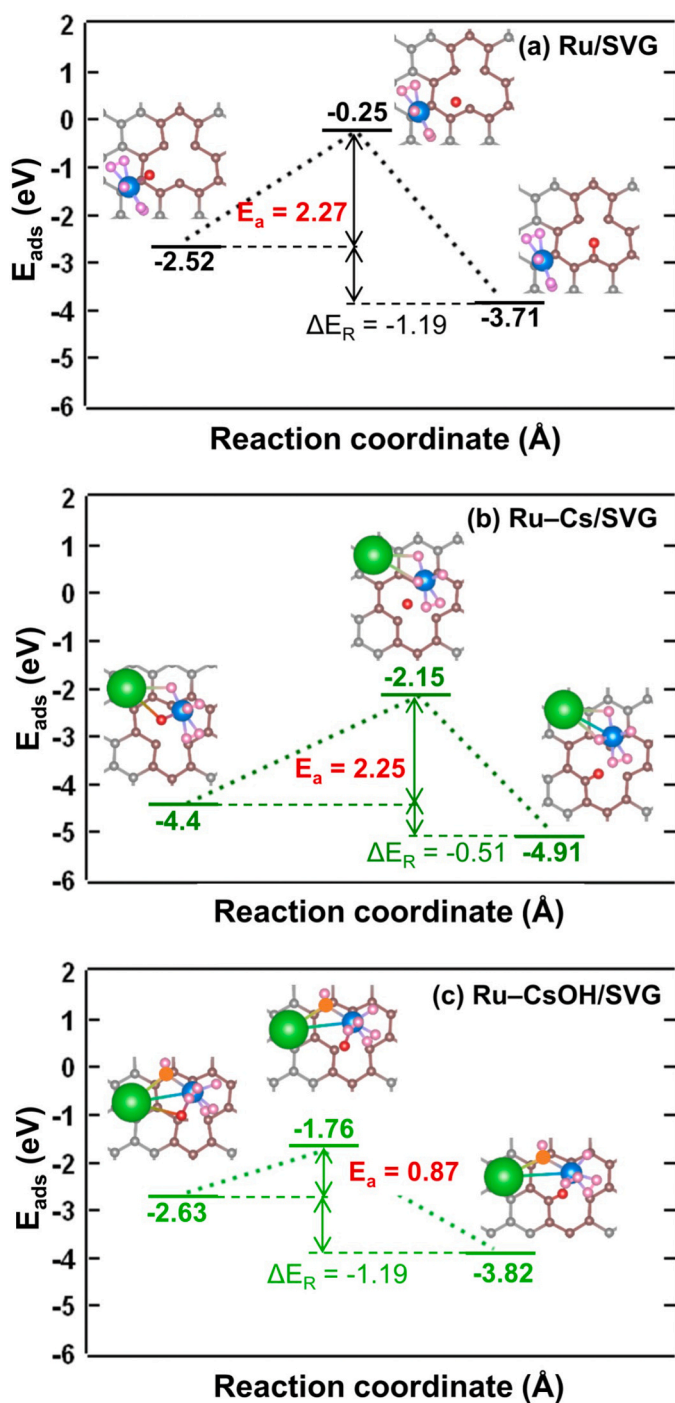
Fig. 13. Reaction coordinate diagram of hydrogen spillover from a Ru atom to single-vacancy graphene (SVG) in (a) Ru/SVG, (b) Ru–Cs/SVG, and (c) Ru–CsOH/SVG models with hydrogen saturated at an Ru/H ratio of 1:6. E_a refers to the activation energy for hydrogen spillover from non-spillover models to spillover models through transition states (structures shown on the left, right, and middle in each image, respectively). ΔE_R refers to the reaction energy between non-spillover and spillover models. Blue, Ru; pink, H; red, spilled-over H; green, Cs; orange, O; gray, C atom away from the C point defect; brown, C atom close to the C point defect.

– review & editing. **Wang Li-Yu:** Formal analysis, Investigation, Visualization. **Yang Chia-Min:** Conceptualization, Funding acquisition, Methodology, Project administration, Supervision, Writing – original draft, Writing – review & editing, Resources. **Chen Shih-Yuan:** Conceptualization, Formal analysis, Methodology, Project

administration, Resources, Supervision, Writing – original draft, Writing – review & editing, Funding acquisition. **Yeh Cheng-Hsi:** Formal analysis, Investigation, Visualization. **Chen Kai-Chun:** Formal analysis, Investigation, Visualization. **Hsiao Wei-Chih:** Formal analysis, Investigation, Visualization. **Liao Chien-Neng:** Formal analysis, Investigation, Methodology. **Chen Hsin-Yu:** Formal analysis, Investigation, Visualization.

Declaration of Competing Interest

The authors declare that they have no known competing financial interests or personal relationships that could have appeared to influence the work reported in this paper.

Data Availability

Data will be made available on request.

Appendix A. Supporting information

Supplementary data associated with this article can be found in the online version at doi:10.1016/j.apcatb.2024.123725.

References

[1] S. Giddey, S.P.S. Badwal, C. Munnings, M. Dolan, Ammonia as a renewable energy transportation media, ACS Sustain. Chem. Eng. 5 (2017) 10231–10239, https://doi.org/10.1021/acssuschemeng.7b02219.
[2] A. Klerke, C.H. Christensen, J.K. Nørskov, T. Vegge, Ammonia for hydrogen storage: challenges and opportunities, J. Mater. Chem. 18 (2008) 2304–2310, https://doi.org/10.1039/B720020J.
[3] F. Schüth, R. Palkovits, R. Schlögl, D.S. Su, Ammonia as a possible element in an energy infrastructure: catalysts for ammonia decomposition, Energy Environ. Sci. 5 (2012) 6278–6289, https://doi.org/10.1039/C2EE02865D, https://doi.org/10.1016/j.apcata.2004.09.020.
[4] S.F. Yin, B.Q. Xu, X.P. Zhou, C.T. Au, A mini-review on ammonia decomposition catalysts for on-site generation of hydrogen for fuel cell applications, Appl. Catal., A 277 (2004) 1–9.
[5] X. Liu, A. Elgowainy, M. Wang, Life cycle energy use and greenhouse gas emissions of ammonia production from renewable resources and industrial by-products, Green. Chem. 22 (2020) 5751–5761, https://doi.org/10.1039/D0GC02301A.
[6] R. Nayak-Luke, R. Bañāres-Alcántara, I. Wilkinson, "Green" ammonia: impact of renewable energy intermittency on plant sizing and levelized cost of ammonia, Ind. Eng. Chem. Res 57 (2018) 14607–14616, https://doi.org/10.1021/acs.iecr.8b02447.

[7] I. Dincer, C. Acar, Review and evaluation of hydrogen production methods for better sustainability, Int. J. Hydrog. Energy 40 (2015) 11094–11111, https://doi.org/10.1016/j.ijhydene.2014.12.035.

[8] D.B. Levin, R. Chahine, Challenges for renewable hydrogen production from biomass, Int. J. Hydrog. Energy 35 (2010) 4962–4969, https://doi.org/10.1016/j.ijhydene.2009.08.067.

[9] K.-I. Aika, A. Ozaki, Kinetics and isotope effect of ammonia synthesis over ruthenium, J. Catal. 16 (1970) 97–101, https://doi.org/10.1016/0021-9517(70)90200-9.

[10] K.-i Aika, T. Takano, S. Murata, Preparation and characterization of chlorine-free ruthenium catalysts and the promoter effect in ammonia synthesis: 3. A magnesia-supported ruthenium catalyst, J. Catal. 136 (1992) 126–140, https://doi.org/10.1016/0021-9517(92)90112-U.

[11] D.E. Brown, T. Edmonds, R.W. Joyner, J.J. McCarroll, S.R. Tennison, The genesis and development of the commercial BP doubly promoted catalyst for ammonia synthesis, Catal. Lett. 144 (2014) 545–552, https://doi.org/10.1007/s10562-014-1226-4.

[12] K.-i Aika, J. Yamaguchi, A. Ozaki, Ammonia synthesis over rhodium, iridium and platinum promoted by potassium, Chem. Lett. 2 (1973) 161–164, https://doi.org/10.1246/cl.1973.161.

[13] K.-i Aika, H. Hori, A. Ozaki, Activation of nitrogen by alkali metal promoted transition metal I. Ammonia synthesis over ruthenium promoted by alkali metal, J. Catal. 27 (1972) 424–431, https://doi.org/10.1016/0021-9517(72)90179-0.

[14] K.S.R. Rao, S.K. Masthan, P.S.S. Prasad, P.K. Rao, Effect of barium addition on the ammonia synthesis activity of a caesium promoted ruthenium catalyst supported on carbon-covered alumina (CCA), Appl. Catal. 73 (1991) L1–L5, https://doi.org/10.1016/0166-9834(91)85104-4.

[15] Z. Kowalczyk, J. Sentek, S. Jodzis, E. Mizera, J. Góralski, T. Paryjczak, R. Diduszko, An alkali-promoted ruthenium catalyst for the synthesis of ammonia, supported on thermally modified active carbon, Catal. Lett. 45 (1997) 65–72, https://doi.org/10.1023/A:1018970318628.

[16] H.-B. Chen, J.-D. Lin, Y. Cai, X.-Y. Wang, J. Yi, J. Wang, G. Wei, Y.-Z. Lin, D.-W. Liao, Novel multi-walled nanotubes-supported and alkali-promoted Ru catalysts for ammonia synthesis under atmospheric pressure, Appl. Surf. Sci. 180 (2001) 328–335, https://doi.org/10.1016/S0169-4332(01)00374-9.

[17] I. Rossetti, N. Pernicone, L. Forni, Graphitised carbon as support for Ru/C ammonia synthesis catalyst, Catal. Today 102–103 (2005) 219–224, https://doi.org/10.1016/j.cattod.2005.02.010.

[18] X. Peng, X. Chen, Y. Zhou, F. Sun, T. Zhang, L. Zheng, L. Jiang, X. Wang, Size-dependent activity of supported Ru catalysts for ammonia synthesis at mild conditions, J. Catal. 408 (2022) 98–108, https://doi.org/10.1016/j.jcat.2022.02.024.

[19] W. Jiang, Y. Li, W. Han, Y. Zhou, H. Tang, H. Liu, Effect of the graphitic degree of carbon supports on the catalytic performance of ammonia synthesis over Ba-Ru-K/HSGC catalyst, J. Energy Chem. 23 (2014) 443–452, https://doi.org/10.1016/S2095-4956(14)60170-4.

[20] J. Ni, S. Shi, C. Zhang, B. Fang, X. Wang, J. Lin, S. Liang, B. Lin, L. Jiang, Enhanced catalytic performance of the carbon-supported Ru ammonia synthesis catalyst by an introduction of oxygen functional groups via gas-phase oxidation, J. Catal. 409 (2022) 78–86, https://doi.org/10.1016/j.jcat.2022.03.026.

[21] M. Nishi, S.-Y. Chen, H. Takagi, X-ray absorption spectroscopy of Ba- and Cs-promoted Ru/mesoporous carbon catalysts for long-term ammonia synthesis under intermittent operation conditions, Sustain. Energy Fuels 4 (2020) 832–842, https://doi.org/10.1039/C9SE00781D.

[22] J. Zheng, F. Liao, S. Wu, G. Jones, T.-Y. Chen, J. Fellowes, T. Sudmeier, I. J. McPherson, I. Wilkinson, S.C.E. Tsang, Efficient non-dissociative activation of dinitrogen to ammonia over lithium-promoted ruthenium nanoparticles at low pressure, Angew. Chem. Int. Ed. 58 (2019) 17335–17341, https://doi.org/10.1002/anie.201907171.

[23] M. Nishi, S.-Y. Chen, H. Tateno, T. Mochizuki, H. Takagi, T. Nanba, A super-growth carbon nanotubes-supported, Cs-promoted Ru catalyst for 0.1–8 MPaG ammonia synthesis, J. Catal. 413 (2022) 623–635, https://doi.org/10.1016/j.jcat.2022.07.015.

[24] K.-i Aika, T. Kawahara, S. Murata, T. Onishi, Promoter effect of alkali-metal oxides and alkali earth metal-oxides on active carbon-supported ruthenium catalyst for ammonia synthesis, Bull. Chem. Soc. Jpn 63 (1990) 1221–1225, https://doi.org/10.1246/bcsj.63.1221.

[25] K.-i Aika, Heterogeneous catalysis of ammonia synthesis at room temperature and atmospheric pressure, Angew. Chem. Int. Ed. 25 (1986) 558–559, https://doi.org/10.1002/anie.198605581.

[26] Y. Zhang, J. Li, J. Cai, L. Yang, T. Zhang, J. Lin, X. Wang, C. Chen, L. Zheng, C.-T. Au, ACS Catal. 11 (2021) 4430–4440, https://doi.org/10.1021/acscatal.0c05544.

[27] L. Li, Y.-F. Jiang, T. Zhang, H. Cai, Y. Zhou, B. Lin, X. Lin, Y. Zheng, L. Zheng, X. Wang, Chem 8 (2022) 749–768, https://doi.org/10.1016/j.chempr.2021.11.008.

[28] W. Raróg, Z. Kowalczyk, J. Sentek, D. Składanowski, J. Zieliński, Effect of K, Cs and Ba on the kinetics of NH3 synthesis over carbon-based ruthenium catalysts, Catal, Letters 68 (2000) 163–168, https://doi.org/10.1023/a:1019024629261.

[29] S.E. Siporin, R.J. Davis, Isotopic transient analysis of ammonia synthesis over Ru/MgO catalysts promoted by cesium, barium, or lanthanum, J. Catal. 222 (2004) 315–322, https://doi.org/10.1016/j.jcat.2003.10.018.

[30] L. Forni, D. Molinari, I. Rossetti, N. Pernicone, Carbon-supported promoted Ru catalyst for ammonia synthesis, Appl. Catal. A 185 (1999) 269–275, https://doi.org/10.1016/S0926-860X(99)00144-1.

[31] I. Rossetti, N. Pernicone, L. Forni, Promoters effect in Ru/C ammonia synthesis catalyst, Appl. Catal. A 208 (2001) 271–278, https://doi.org/10.1016/S0926-860X(00)00711-0.

[32] S.-Y. Chen, L.-Y. Jang, S. Cheng, Synthesis of Zr-incorporated SBA-15 mesoporous materials in a self-generated acidic environment, Chem. Mater. 16 (2004) 4174–4180, https://doi.org/10.1021/cm049247b.

[33] C.-M. Yang, B. Zibrowius, W. Schmidt, F. Schüth, Stepwise removal of the copolymer template from mesopores and micropores in SBA-15, Chem. Mater. 16 (2004) 2918–2925, https://doi.org/10.1021/cm049526z.

[34] P.-H. Ku, C.-Y. Hsiao, M.-J. Chen, T.-H. Lin, Y.-T. Li, S.-C. Liu, K.-T. Tang, D.-J. Yao, C.-M. Yang, Polymer/ordered mesoporous carbon nanocomposite platelets as superior sensing materials for gas detection with surface acoustic wave devices, Langmuir 28 (2012) 11639–11645, https://doi.org/10.1021/la3015892.

[35] S. Jun, S.H. Joo, R. Ryoo, M. Kruk, M. Jaroniec, Z. Liu, T. Ohsuna, O. Terasaki, Synthesis of new, nanoporous carbon with hexagonally ordered mesostructure, J. Am. Chem. Soc. 122 (2000) 10712–10713, https://doi.org/10.1021/ja002261e.

[36] M. Kruk, M. Jaroniec, T.-W. Kim, R. Ryoo, Synthesis and characterization of hexagonally ordered carbon nanopipes, Chem. Mater. 15 (2003) 2815–2823, https://doi.org/10.1021/cm034087+.

[37] A.M. Beale, B.M. Weckhuysen, EXAFS as a tool to interrogate the size and shape of mono and bimetallic catalyst nanoparticles, Phys. Chem. Chem. Phys. 12 (2010) 5562–5574, https://doi.org/10.1039/B925206A.

[38] C.-H. Wang, S.-T. Chang, S.-Y. Chen, Y.-W. Yang, New ambient pressure X-ray photoelectron spectroscopy endstation at Taiwan light source, AIP Conf. Proc. 2054 (2019) 040012, https://doi.org/10.1063/1.5084613.

[39] J.P. Perdew, K. Burke, M. Ernzerhof, Generalized gradient approximation made simple, Phys. Rev. Lett. 77 (1996) 3865–3868, https://doi.org/10.1103/PhysRevLett.77.3865.

[40] G. Kresse, J. Furthmüller, Efficiency of ab-initio total energy calculations for metals and semiconductors using a plane-wave basis set, Comput. Mater. Sci. 6 (1996) 15–50, https://doi.org/10.1016/0927-0256(96)00008-0.

[41] P.E. Blöchl, Projector augmented-wave method, Phys. Rev. B 50 (1994) 17953–17979, https://doi.org/10.1103/PhysRevB.50.17953.

[42] G. Kresse, D. Joubert, From ultrasoft pseudopotentials to the projector augmented-wave method, Phys. Rev. B 59 (1999) 1758–1775, https://doi.org/10.1103/PhysRevB.59.1758.

[43] S. Grimme, S. Ehrlich, L. Goerigk, Effect of the damping function in dispersion corrected density functional theory, J. Comput. Chem. 32 (2011) 1456–1465, https://doi.org/10.1002/jcc.21759.

[44] S. Grimme, J. Antony, S. Ehrlich, H. Krieg, A consistent and accurate ab initio parametrization of density functional dispersion correction (DFT-D) for the 94 elements H-Pu, J. Chem. Phys. 132 (2010) 154104, https://doi.org/10.1063/1.3382344.

[45] H.J. Monkhorst, J.D. Pack, Special points for Brillouin-zone integrations, Phys. Rev. B 13 (1976) 5188–5192, https://doi.org/10.1103/PhysRevB.13.5188.

[46] D. Sheppard, P. Xiao, W. Chemelewski, D.D. Johnson, G. Henkelman, A generalized solid-state nudged elastic band method, J. Chem. Phys. 136 (2012) 074103, https://doi.org/10.1063/1.3684549.

[47] Z.Q. Li, C.J. Lu, Z.P. Xia, Y. Zhou, Z. Luo, X-ray diffraction patterns of graphite and turbostratic carbon, Carbon 45 (2007) 1686–1695, https://doi.org/10.1016/j.carbon.2007.03.038.

[48] W.J. Sagues, A. Jain, D. Brown, S. Aggarwal, A. Suarez, M. Kollman, S. Park, D. S. Argyropoulos, Are lignin-derived carbon fibers graphitic enough? Green. Chem. 21 (2019) 4253–4265, https://doi.org/10.1039/C9GC01806A.

[49] C. Hu, S. Sedghi, A. Silvestre-Albero, G.G. Andersson, A. Sharma, P. Pendleton, F. Rodríguez-Reinoso, K. Kaneko, M.J. Biggs, Raman spectroscopy study of the transformation of the carbonaceous skeleton of a polymer-based nanoporous carbon along the thermal annealing pathway, Carbon 85 (2015) 147–158, https://doi.org/10.1016/j.carbon.2014.12.098.

[50] A.C. Ferrari, J. Robertson, Interpretation of Raman spectra of disordered and amorphous carbon, Phys. Rev. B 61 (2000) 14095–14107, https://doi.org/10.1103/PhysRevB.61.14095.

[51] A. Sadezky, H. Muckenhuber, H. Grothe, R. Niessner, U. Pöschl, Raman microspectroscopy of soot and related carbonaceous materials: spectral analysis and structural information, Carbon 43 (2005) 1731–1742, https://doi.org/10.1016/j.carbon.2005.02.018.

[52] M.W. Smith, I. Dallmeyer, T.J. Johnson, C.S. Brauer, J.-S. McEwen, J.F. Espinal, M. Garcia-Perez, Structural analysis of char by Raman spectroscopy: improving band assignments through computational calculations from first principles, Carbon 100 (2016) 678–692, https://doi.org/10.1016/j.carbon.2016.01.031.

[53] R. Janus, A. Wach, P. Kuśtrowski, B. Dudek, M. Drozdek, A.M. Silvestre-Albero, F. Rodríguez-Reinoso, P. Cool, Investigation on the low-temperature transformations of poly(furfuryl alcohol) deposited on MCM-41, Langmuir 29 (2013) 3045–3053, https://doi.org/10.1021/la3041852.

[54] S.-Y. Chen, C.-L. Chang, M. Nishi, W.-C. Hsiao, Y.I.A. Reyes, H. Tateno, H.-H. Chou, C.-M. Yang, H.-Y.T. Chen, T. Mochizuki, H. Takagi, T. Nanba, Unraveling the active sites of Cs-promoted Ru/γ-Al2O3 catalysts for ammonia synthesis, Appl. Catal. B 310 (2022) 121269, https://doi.org/10.1016/j.apcatb.2022.121269.

[55] M. Nishi, S.-Y. Chen, H. Takagi, Energy efficient and intermittently variable ammonia synthesis over mesoporous carbon-supported Cs-Ru nanocatalysts, Catalysts 9 (2019) 406, https://doi.org/10.3390/catal9050406.

[56] K.-i Aika, K. Inazu, M. Sugimoto, Hysteresis in ammonia catalysis: comparison between iron and ruthenium catalysts, The 9th Tokyo Conference on Advanced Catalytic Science and Technology, Fukuoka, Japan, July 24–29, 2022.

[57] W. Raróg-Pilecka, E. Miśkiewicz, S. Jodzis, J. Petryk, D. Łomot, Z. Kaszkur, Z. Karpiński, Z. Kowalczyk, Carbon-supported ruthenium catalysts for NH3

synthesis doped with caesium nitrate: activation process, working state of Cs–Ru/C, J. Catal. 239 (2006) 313–325, https://doi.org/10.1016/j.jcat.2006.01.035.

[58] I. Rossetti, L. Sordelli, P. Ghigna, S. Pin, M. Scavini, L. Forni, EXAFS-XANES evidence of in situ cesium reduction in Cs-Ru/C catalysts for ammonia synthesis, Inorg. Chem. 50 (2011) 3757–3765, https://doi.org/10.1021/ic2001656.

[59] J.L. Eslava, A. Iglesias-Juez, G. Agostini, M. Fernandez-Garcia, A. Guerrero-Ruiz, I. Rodriguez-Ramos, Time-resolved XAS investigation of the local environment and evolution states of a Fischer–Tropsch Ru–Cs/C catalyst, ACS Catal. 6 (2016) 1437–1445, https://doi.org/10.1021/acscatal.5b02489.

[60] S.-J. Yang, C.W. Bates Jr., The role of cesium suboxides in low-work-function surface layers studied by x-ray photoelectron spectroscopy: Ag-O-Cs, Appl. Phys. Lett. 36 (1980) 675–677, https://doi.org/10.1063/1.91620.

[61] E.A. Podgornov, I.P. Prosvirin, V.I. Bukhtiyarov, XPS, TPD and TPR studies of Cs–O complexes on silver: their role in ethylene epoxidation, J. Mol. Catal. A: Chem. 158 (2000) 337–343, https://doi.org/10.1016/S1381-1169(00)00101-1.

[62] Y.V. Larichev, I.P. Prosvirin, D.A. Shlyapin, N.B. Shitova, P.G. Tsyrul`nikov, V.I. Bukhtiyarov, An XPS study of the promotion of Ru-Cs/Sibunit catalysts for ammonia synthesis, Kinet. Catal. 46 (2005) 597–602, https://doi.org/10.1007/s10975-005-0113-9.

[63] Y.V. Larichev, B.L. Moroz, V.I. Zaikovskii, S.M. Yunusov, E.S. Kalyuzhnaya, V.B. Shur, V.I. Bukhtiyarov, XPS and TEM studies on the role of the support and alkali promoter in Ru/MgO and Ru–Cs$^+$/MgO catalysts for ammonia synthesis, J. Phys. Chem. C. 111 (2007) 9427–9436, https://doi.org/10.1021/jp066970b.

[64] D.J. Morgan, Resolving ruthenium: XPS studies of common ruthenium materials, Surf. Interface Anal. 47 (2015) 1072–1079, https://doi.org/10.1002/sia.5852.

[65] T. Szabó, O. Berkesi, P. Forgó, K. Josepovits, Y. Sanakis, D. Petridis, I. Dékány, Evolution of surface functional groups in a series of progressively oxidized graphite oxides, Chem. Mater. 18 (2006) 2740–2749, https://doi.org/10.1021/cm060258.

[66] Y.M. Shulga, S.A. Baskakov, E.I. Knerelman, G.I. Davidova, E.R. Badamshina, N.Y. Shulga, E.A. Skryleva, A.L. Agapov, D.N. Voylov, A.P. Sokolov, V.M. Martynenko, Carbon nanomaterial produced by microwave exfoliation of graphite oxide: new insights, RSC Adv. 4 (2014) 587–592, https://doi.org/10.1039/C3RA43612H.

[67] J. Ni, H. Ran, J. Lin, X. Wang, B. Lin, L. Jiang, Investigation on deactivation of K-promoted Ru catalyst for ammonia synthesis by CO formation, ChemistrySelect 5 (2020) 6639–6645, https://doi.org/10.1002/slct.202000772.